Probing Gray Matter Microstructure in Alzheimer's Disease using Diffusion MRI

Teresa Scheidt

LUND
UNIVERSITY

Department of Automatic Control

MSc Thesis
TFRT-6160
ISSN 0280-5316

Department of Automatic Control
Lund University
Box 118
SE-221 00 LUND
Sweden

Printed in Sweden by Tryckeriet i E-huset
Lund 2022

Abstract

Alzheimer's disease is a neurodegenerative disease and the most common cause of dementia. Apart from an early and accurate diagnosis, the ability to track progressive changes is important for the development of disease modifying treatments. Diffusion magnetic resonance imaging is a potential method to detect the microstructural changes in the gray matter, which appear years prior to cortical atrophy and clinical symptoms.

In this thesis, multi-tissue constrained spherical deconvolution is used to model three main tissue classes in the brain (gray matter, white matter and cerebral spinal fluid) based on the diffusion signal. By comparing the tissue fractions in healthy elderly with patients in different stages of the Alzheimer's disease spectrum using gray matter based spatial statistics, this work demonstrates the potential of the tissue fractions to investigate microstructural changes. The gray matter fraction was lower in patients on the AD spectrum, while the cerebral spinal fluid fraction was higher. These differences are in line with the expected results and appear in pathological affected areas. Compared to another diffusion based metric (mean diffusivity) the tissue fractions showed a higher sensitivity and detected differences in an earlier stage. Overall, this indicates the high potential of these metrics to detect early microstructural changes in Alzheimer's disease.

Acknowledgements

This thesis was done at the MR Physics group at Lund University. I would like to thank everyone from the group for your warm welcome and your valuable feedback on my work. I really enjoyed my time during my thesis here and I am looking forward to working with you in the future!

Special thanks to my supervisors, Nicola and Markus. Thank you for introducing me to this very interesting topic and your continuous support during the last months. I learned so much from you, thank you for taking the time to explain everything and providing me with new ideas.

I also want to thank Geraline for explaining the software to me and running certain preprocessing steps, this saved me many days of frustration and waiting.

Last but not least, I want to thank my boyfriend Tobias. Thank you for your endless support and love during the last years! And of course for reading my thesis over and over again and giving me feedback on every little detail.

Abbreviations

A	Amyloid beta
Aβ	Amyloid beta
AD	Alzheimer's disease
CSD	Constrained spherical deconvolution
CSF	Cerebral spinal fluid
CTh	Cortical thickness
dMRI	Diffusion magnetic resonance imaging
DTI	Diffusion tensor imaging
FA	Fractional anisotropy
FWE	Family-wise error
GBSS	Gray matter-based spatial statistics
GM	Gray matter
MCI	Mild cognitive impairment
MD	Mean diffusivity
MD_{nocsf}	Mean diffusivity without CSF signal
MRI	Magnetic resonance imaging
MT-CSD	Multi-tissue constrained spherical deconvolution
NODDI	Neurite orientation dispersion and density imaging
PET	Positron emission tomography
RF	Radio-frequency
ROI	Region of interest
SH	Spherical harmonics
T	Tau
VBM	Voxel-based morphometry
WM	White matter

Contents

1. Introduction **11**
- 1.1 Background . . . 11
- 1.2 Aim of the Thesis . . . 11

2. Background **13**
- 2.1 The brain . . . 13
- 2.2 Alzheimer's Disease . . . 14
- 2.3 Magnetic Resonance Imaging . . . 17
- 2.4 Diffusion-Weighted Imaging . . . 18
- 2.5 Models . . . 21
- 2.6 Statistical Evaluation . . . 25

3. Motivation **28**
- 3.1 Current Biomarkers . . . 28
- 3.2 Use of MT-CSD and GBSS . . . 29

4. Methods **30**
- 4.1 Data . . . 30
- 4.2 Software . . . 31
- 4.3 Pipeline . . . 32
- 4.4 Statistical Evaluation . . . 39
- 4.5 Simulation . . . 40

5. Results **42**
- 5.1 Voxel-wise Analysis . . . 42
- 5.2 Region-based analysis . . . 45
- 5.3 Simulation . . . 47

6. Discussion **49**

7. Conclusion **54**

Bibliography **55**

A. Image artifacts **62**
- A.1 Denoising . . . 62
- A.2 Gibbs Artifact Removal . . . 62
- A.3 Susceptibility-induced Distortions Correction . . . 63

A.4 Motion and Eddy Correction 64
A.5 Bias Field Correction 64
B. Additional results **66**

1

Introduction

1.1 Background

Alzheimer's disease (AD) is the most common cause of dementia among elderly. With an aging population, the prevalence of neurodegenerative diseases, like AD, is rising. This makes AD and dementia research essential to improve the lives of millions. Within AD research, a timely and accurate diagnosis as well as the ability of following the progression of the disease is of utter importance. AD pathology starts up to two decades before clinical symptoms appear, so an early diagnosis is vital for the development of future treatments [70]. To investigate the progression of the disease and the potential effects of treatments, it is important to be able to track the changes in the brain. One way of tracking structural changes is to use magnetic resonance imaging (MRI).

MRI is a medical imaging method that utilizes the magnetic resonance of protons and works with a strong magnetic field. It provides great contrast of soft tissues like the brain. It can be used to access structural information and is used to detect atrophy of the brain in AD. However, microstructural changes are thought to appear prior to structural changes [73]. One potential method to detect these microstructural changes is diffusion MRI (dMRI). By measuring the extent and direction of diffusion of water molecules, dMRI can give insight into microstructural properties of the tissue. In AD the microstructure is expected to change due to pathological processes. Observing and quantifying these changes can provide insight into the disease process and help in testing the effect of up-coming disease modifying therapies. Several dMRI methods have already shown the potential to detect microstructural changes prior to cortical thinning and atrophy [74, 72].

1.2 Aim of the Thesis

The aim of this thesis is to investigate methods that could lead to potential biomarkers based on dMRI for monitoring the disease progression of AD, by detecting microstructural changes in gray matter (GM). This thesis will focus on the GM microstructure since AD in its early stage mainly affects the cortex [10]. To accomplish

this goal, relevant literature was reviewed in detail to identify metrics of interest and applicable methods. This review resulted in two main methods:

- Use of multi tissue constrained spherical deconvolution (MT-CSD) [32] to extract tissue fractions as potential biomarkers.
- Use of gray matter-based spatial statistics (GBSS) [44] for skeletonization of the GM and subsequent group-wise comparisons between healthy controls and patients with AD in early stages.

MT-CSD is a signal-based model, which models the three main tissue classes in the brain (GM, white matter (WM) and cerebral spinal fluid (CSF)) based on the diffusion signal. By accessing the different tissue fractions, potential changes in the microstructure can be investigated. GBSS is used to skeletonize the GM and enable a group-wise comparison. The GBSS pipeline will be altered to work based on MT-CSD. The main metrics of interest are GM and CSF fraction and they will be compared to current state-of-the-art biomarkers. This thesis aims to investigate if these metrics could be a potential marker for detecting microstructural changes in the GM in the AD spectrum.

2

Background

This chapter gives an introduction to Alzheimer's disease and diffusion MRI. Furthermore, an overview of the main methods used in this thesis is given.

2.1 The brain

The brain is part of the central nervous system and processes sensory input, controls motor skills and regulates our body function. The brain is also the center of learning, thought and memory.

The brain consists of billions of neurons, which have a cell body (soma), dendrites and a long axon that is often covered in myelin (Fig. 2.1). On a structural level, the brain is divided into different tissue classes, gray matter and white matter. These tissues differ in cell composition and the macro- and microstructural organization. Gray matter consists mainly of soma, dendrites and unmyelinated axons while the white matter contains the myelinated axons mostly arranged in bundles. There are also other types of cells, e.g. glia cells, present. The outer layer of the brain, the cortex, consists of gray matter and is responsible for most of the information processing. The cerebral cortex is between 1 and 4.5 mm thick [25].

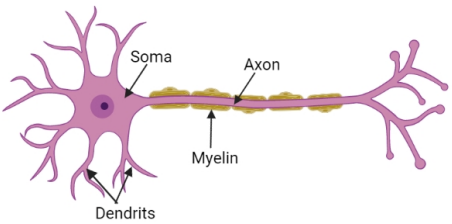

Figure 2.1 Schema of a neuron.

Generally, the brain can be divided into the cerebrum, the cerebellum and the brain stem. The cerebral cortex is the outer layer of the cerebrum, which can be

further divided into four lobes: frontal, parietal, temporal and occipital lobe (see Fig. 2.2). Each lobe has a different function, the temporal lobe for example is mainly responsible for short-term memory and speech. At the base of the temporal lobes lies the hippocampus, which supports among others memory and learning.

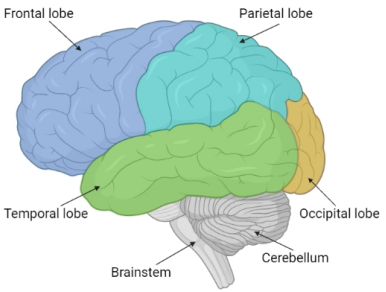

Figure 2.2 Anatomy of the human brain.

2.2 Alzheimer's Disease

General

AD is a neurodegenerative disorder and the most common cause of dementia. Currently, around 50 million people are affected by dementia, where AD accounts for 60-70% of cases [27]. Symptoms of AD include memory impairment, difficulties with language, problems with vision and spatial issues as well as impaired reasoning or judgment. The causes of AD are not fully understood, but age-related processes, as well as genetic and environmental risk factors, seem to play a role in the development of AD. Recent studies show that AD pathology starts two decades before patients show the first symptoms [70], so an early diagnosis (before clinical symptoms appear) is vital for treatment and a precise diagnosis is needed for clinical trials. Currently, AD is not curable but many disease-modifying treatments are being tested.

Mild cognitive impairment (MCI) can be an early sign of AD. MCI is a condition of memory problems and patients with MCI have a greater risk of developing AD. However, AD is not the only cause of MCI and in many cases, MCI does not lead to dementia and the symptoms of MCI stay the same or can even improve over time. For inclusion in AD studies, it is important to diagnose the cause of MCI correctly.

Cellular Mechanisms

The exact causes and cellular mechanisms of AD are not yet fully understood. But the pathology of AD is defined by two major cellular abnormalities occurring, the accumulation of Aβ protein and neuronal neurofibrillary tangles containing hyperphosphorylated tau proteins. The typical pattern of progression of Aβ and tau pathologies in the brain are different from each other, as it can be seen in Fig. 2.3. Aβ accumulation starts in the neocortex in medial parietal and frontal areas and later occurs in other cortical areas. The brainstem and cerebellum are affected last. Tau accumulation starts occurring in the medial temporal structure, and later in the hippocampus and the neocortex.

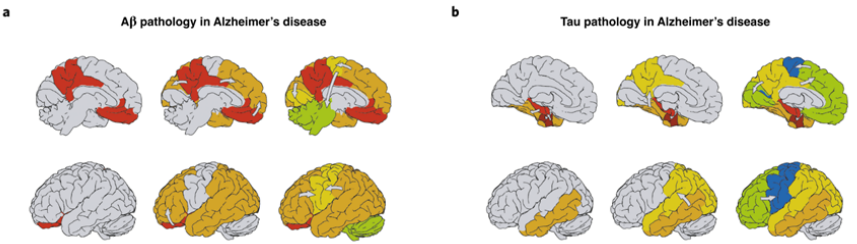

Figure 2.3 Progression of AD pathology in the brain. **a** Aβ accumulation starts in the neocortex in medial parietal and frontal areas (red) and then occurs in other cortical areas (orange, yellow). The brainstem and cerebellum are affected last (green). **b** Tau-tangles start occurring in the entorhinal cortex (dark-red), followed by the hippocampus (red) and then to the temporal lobe (orange) and to the neocortex (yellow). Frontal areas (green) and the motor and sensory areas (blue) are affected last. Image and description from [27].

Aβ is derived from the transmembrane amyloid precursor protein which is concentrated in neuronal synapses. This protein is broken down into the Aβ peptide, which contains 37-43 amino acids. Especially the longer Aβ42 and Aβ43 tend to aggregate, forming Aβ fibrils that are the main component of plaques found in AD. There are theories that Aβ drives the tau pathology and neurodegeneration [28]. Studies have shown that Aβ accumulation starts about 20 years before dementia onset in AD [70].

Tau is a microtubuli binding protein located mainly in the axons stabilizing the microtubuli (and therefore the axons). In AD, tau detaches from the microtubuli due to misfolding of the protein and accumulates, which ultimately leads to cell death and neurodegeneration. It is still unknown what causes the tau pathology and how exactly it spreads.

These two proteins are the main target for disease modifying therapies. The detection of these proteins is an important biomarker to diagnose the disease. The importance of biomarkers is elaborated further in the next section.

Biomarkers

Biomarkers for AD are used to diagnose and stage the disease and are crucial for the development and monitoring of the response to therapies during clinical trials. According to the National Institute on Aging - Alzheimer's Association Research Framework [30] biomarkers for AD can be classified in three groups: markers that detect Aβ, tau and neuronal injury and neurodegeneration. From these pathologies Aβ occurs first, followed by tau and changes in the brain macrostructure (atrophy, degeneration, shrinkage) which tend to be detectable close to the onset of clinical symptoms (see Fig. 2.4). It is hypothesized that before macrostructural changes of the brain become visible in structural MRI scans, microstructural changes take place (earliest in GM), which might be detectable with dMRI (see Chapter 2.4). The detection of microstructural changes is the focus of this thesis, which could lead to earlier detection of neurodegenerative changes [73].

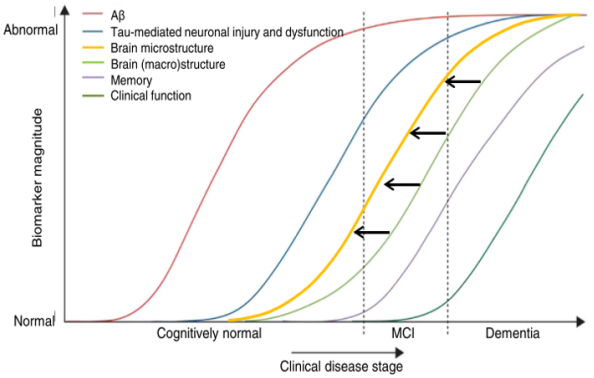

Figure 2.4 Sequence of biomarker changes in AD. Aβ pathology appears first, followed by tau pathology and changes in the brain structure. Clinical symptoms appear last, well into the progression of AD. The arrows indicate how the use of dMRI (for detection of microstructural changes) could lead to earlier detection of structural changes in the brain before macrostructural changes become visible. Image from [73].

Markers of Aβ and tau are used to define the disease, so they are important for a timely and specific diagnosis and inclusion in clinical trials. They also have the potential to predict the disease progression [34, 47, 53]. Currently, the clinical diagnosis of AD is strongly supported by the detection of these proteins in the CSF, plasma or with positron emission tomography (PET) [24, 37, 50].

Markers of neurodegeneration are used to stage the disease and its progression and include for example the atrophy of the brain. The most commonly used metric in this context is the cortical thickness (CTh), which can be measured using structural MRI scans. Over the progression of the disease, the cortex will degener-

ate, which becomes visible in thinning of the cortex. The areas of cortical thinning align with the known regions affected by AD pathology [22]. However, these degenerative changes are thought to appear years after the pathological changes of Aβ and tau [70]. With the use of dMRI, it might be possible to detect microstructural changes in the brain that occur prior to atrophy. These microstructural changes are expected to occur first in GM, as AD is primarily a cortical disease in its early stages [10]. Recent studies have shown the potential of dMRI based biomarkers to detect microstructural changes prior to cortical atrophy [72, 74].

A more comprehensive overview of the use of dMRI in AD research is given in Chapter 3.

2.3 Magnetic Resonance Imaging

MRI is an imaging technique that uses a strong magnetic field and in contrast to other imaging techniques, like computed tomography, no ionizing radiation. Instead, it leverages the behavior of spins of protons (nucleus of the hydrogen atom) under a magnetic field. It is especially well suited to show soft tissues, thanks to the high hydrogen content in water and fat. In the brain, GM and WM can be differentiated with MRI.

Underlying Principles

In a strong external magnetic field of an MRI scanner, protons align with the magnetic field (B_0), resulting in a longitudinal magnetization along the B_0 field. The protons spin at a frequency (Lamor frequency), which is linearly dependent on B_0 and leads to a rotating magnetization. If a radio-frequency pulse (RF-pulse) at Larmor frequency is applied, the magnetization is moved into the transverse plane (perpendicular to the B_0 field), which can than be measured by conductive coils.

After the application of the RF-pulse, relaxations take place in two principally different ways: the protons fall out of phase (T2 relaxation), which leads to the transverse magnetization disappearing, and the protons return to the lower energy state (T1 relaxation), which causes the longitudinal magnetization to grow back. These relaxations occur at different speeds depending on the bond of the hydrogen atoms, which makes it possible to differentiate between free water and different tissues. For example, the T1 relaxation in fat is faster than in water and the T2 value in free water is longer than in water-based tissues [16]. Images can be T1 or T2-weighted by altering the pulse repetition time and the echo time.

The structural dephasing[1] of protons can be reversed by applying a second RF-pulse, which flips the protons by 180°. The protons will continue to dephase at the same rate, leading to the protons being in phase again at the time for read-out, leading to a greater signal. The second RF-pulse should be applied at half the echo

[1] random dephasing can not be reversed

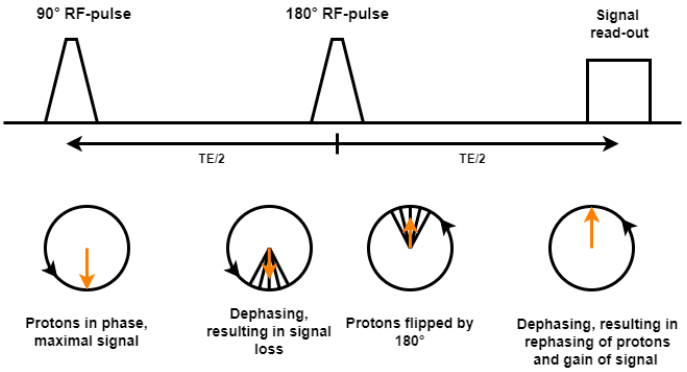

Figure 2.5 Use of spin-echo to maximize signal by rephasing protons. On the top the pulse sequence is depicted. The bottom shows the dephasing and rephasing of protons leading to signal loss or restoration respectively. TE = echo time.

time to have the largest signal at the read-out. The pulse sequence and dephasing of protons can be seen in Figure 2.5. This sequence is known as spin-echo sequence and is of great use in diffusion-weighted imaging (see Chapter 2.4).

In order to reconstruct a 3D image from the MR signal, the signal needs to be spatially encoded. This is achieved by applying gradient fields in the three main directions. These gradient fields alter the frequency and phase of the protons depending on their respective positions in the gradient field, which allows for localization of the signal in a 3D plane.

2.4 Diffusion-Weighted Imaging

dMRI leverages the diffusion of water molecules to create diffusion-weighted images, which are sensitive to microstructural properties of the tissue. In any MRI image, there is signal loss due to diffusion of protons. This is caused by the gradient, that alters the phase of protons depending on their position. If the protons move along that gradient, it causes them to be out of phase with neighboring protons, which leads to signal loss. In dMRI this signal loss is used to quantify the diffusion. Diffusion-weighted images can be used to identify areas with changed tissue properties (and therefore changed diffusion), like tumors or infarcts.

Diffusion

Diffusion is the random movement of particles in a medium, also known as Brownian motion [68]. In a free medium without any restriction this movement is Gaussian distributed. The mean-squared displacement of a molecule in free diffusion is de-

fined by

$$\langle x^2 \rangle = 2Dt \tag{2.1}$$

where D describes the diffusion coefficient, which is constant over time in free diffusion, and t is the diffusion time. In three dimensions this equation becomes

$$\langle r^2 \rangle = 6Dt \tag{2.2}$$

In the brain, free diffusion can only be assumed in regions with free water contents, like in CSF, which has the diffusion coefficient of $D_{CSF} = 3\frac{mm^2}{s}$. In tissues the diffusion is restricted and hindered. In extra-cellular space, the diffusion is hindered by cell bodies and axons, which introduces a correlation between random motions if the particle collides with a cell wall. In closed space, like inside of cells, the diffusion is restricted by the cell walls as particles cannot leave the cell[2]. In hindered and restricted diffusion, the diffusion coefficient decreases over time and is lower than in free diffusion.

Diffusion can also be differentiated into isotropic and anisotropic diffusion, which is a useful distinction regarding the brain. Isotropic diffusion means that movements are equally probable in all directions, this is for example the case in CSF or inside the soma (on short time intervals). Anisotropic diffusion refers to diffusion where movements are more or less probable in different directions. For example, in axons the particles are more likely to move along the axons, than perpendicular to them (into cell walls), which is mirrored in different diffusion coefficients depending on the direction of movement. Anisotropic diffusion is mostly present in WM, as WM mainly consists of axon bundles. This property is also utilized to reconstruct the axon tracts of WM by extracting the direction of diffusion. In GM isotropic diffusion, but with a lower diffusion coefficient than in free water, is prevalent, as GM is dominated by cell soma. The apparent diffusivity of GM is around $0.9\frac{mm^2}{s}$ [54].

Utilizing the different types of diffusion, caused by microstructural differences in tissues, information about the microstructure of the brain tissue can be extracted. The applications of dMRI include (but are certainly not limited to) identification of infarcts, reconstruction of pathways of nerve tracts and detection of microstructural changes in the brain, for example caused by aging or disease.

Imaging

Diffusion can be quantified by measuring signal loss, which occurs because of the dephasing of protons caused by movement of the protons. As described earlier, using a spin-echo sequence, dephasing can be reversed leading to restoring of signal. However, the signal could only be completely restored if the protons stayed in the same place, which does not happen due to diffusion. By adding a strong gradient to an MRI sequence, it gets sensitive to diffusion, as it can be seen in Figure 2.6. Protons along the gradient have different phases and if the protons move along this

[2] although this is a simplification that does not take into account e.g., cellular exchange

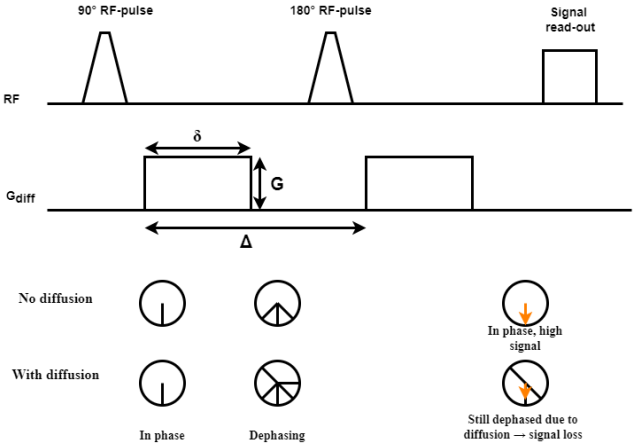

Figure 2.6 Use of spin-echo to image diffusion. Signal from stationary molecules is unaffected, as they rephase. For moving particles signal is lost, due to dephasing caused by the movement and the gradient. Image adapted from [4].

gradient, it leads to stronger dephasing with neighboring protons. This dephasing cannot be reversed by the 180° RF-pulse. The further the proton moves (i.e. the higher the diffusion coefficient) the more it will out of phase with other protons, which leads to a higher signal loss. The relation between the diffusion coefficient and the signal loss is defined by

$$S = S_0 e^{-bD}$$
$$\ln \frac{S}{S_0} = -bD, \tag{2.3}$$

where S is the measured signal, S_0 is the signal without a diffusion gradient and b is a measure of diffusion weighting. The b-value is depended on the amplitude of the gradient field (G), the duration of applied gradients (δ) and the time between two gradients (Δ) and has the unit $\frac{s}{mm^2}$ (G,δ and Δ are visualized in Figure 2.6). It is defined as

$$b = \gamma^2 \delta^2 |G|^2 (\Delta - \frac{\delta}{3}). \tag{2.4}$$

The larger the b-value, the stronger is the diffusion effect, leading to more signal loss. Commonly, b-values around $1000\frac{s}{mm^2}$ are used. The direction of the gradient field is given by the b-vector.

This relation between signal decay and the diffusion coefficient (2.3), enables us to estimate D in each voxel (using space encoding gradients). By applying gradient fields in different directions D can be estimated depending on the direction, giving important information about the microstructure of the tissue (e.g. fiber-orientation in WM).

2.5 Models

Several reconstruction methods use different models to extract information from the dMRI signal. There are signal-based models (e.g. diffusion tensor imaging (DTI) [38], constrained spherical deconvolution (CSD) [66]) and biological models (e.g. neurite orientation dispersion and density imaging (NODDI) [77]). Some of these models are described in more detail in the following sections.

Diffusion Tensor Imaging

DTI [38] is one of the most common methods to model diffusion in the brain. In DTI diffusion is modeled as a tensor

$$\mathbf{D} = \begin{bmatrix} D_{xx} & D_{xy} & D_{xz} \\ D_{yx} & D_{yy} & D_{yz} \\ D_{zx} & D_{zy} & D_{zz} \end{bmatrix}, \tag{2.5}$$

which describes the diffusion in all directions. Given the nature of diffusion, $\mathbf{D}$ is symmetric and positive definite ($D_{xy} = D_{yx}$ and $D > 0$). Using singular eigenvalue decomposition $\mathbf{D}$ can be described by its eigenvalues $\lambda_{1,2,3}$ and eigenvectors $e_{1,2,3}$. The diffusion tensor can be visualized using an ellipsoid, as in Figure 2.7. While isotropic diffusion is represented by a sphere (since D is equal in all directions) with no main direction, anisotropic diffusion has a main direction given by the e_1 (corresponding to the largest eigenvalue λ_1).

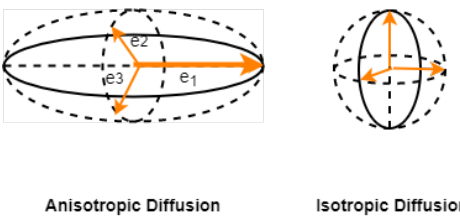

Figure 2.7 Diffusion represented by a diffusion tensor ellipsoid. In anisotropic diffusion a main direction of diffusion is given by e_1, while isotropic diffusion has no main direction and is represented by a sphere.

From the DTI model, different measures can be extracted. Two of the main measures are mean diffusivity (MD) (2.6) and fractional anisotropy (FA) (2.7). MD is linked to tissue properties and differs between GM, WM and CSF. FA describes the fraction of anisotropic diffusion, which is high in WM and very low to zero in GM and CSF. Changes in MD and FA indicated changes in microstructure caused by for example pathological processes.

$$MD = \frac{\lambda_1 + \lambda_2 + \lambda_3}{3} \tag{2.6}$$

$$FA = \sqrt{\frac{(\lambda_1 - \lambda_2)^2 + (\lambda_2 - \lambda_3)^2 + (\lambda_3 - \lambda_1)^2}{2(\lambda_1^2 + \lambda_2^2 + \lambda_3^2)}} \tag{2.7}$$

One main drawback of DTI is that only one principal direction can be modeled per voxel. In reality, voxels may contain crossing fibers that lead to diffusion in two or more main directions. This crossing can not be modeled in DTI and leads to inaccurate directions and less accurate reconstruction of fiber pathways in WM. One approach that solves this problem is described in the next section.

Constrained Spherical Deconvolution

Another way to extract fiber orientations in voxels is spherical deconvolution. It is based on the principle, that the signal is given by the spherical convolution of the response function (signal profile for a certain tissue) with the fiber orientation [64]. This is visualized in Figure 2.8. By performing spherical deconvolution of the measured signal and the response function, the fiber orientation can be estimated. To reduce the susceptibility to noise, the constraint of not allowing negative values (which are physically impossible) is added, giving CSD [66]. CSD is able to model crossing fibres in one voxel without any biological assumptions.

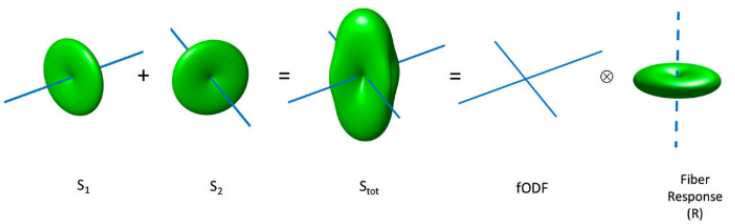

Figure 2.8 Principal of spherical deconvolution. The measuerd signal (S_{tot}) is a combination of the fibre orientations density function (fODF) and the specific fibre response function (R). Image from [17].

The key part of this method is the response function, which is modeled using a spherical harmonics (SH) series. SH form an orthonormal basis for functions on a sphere. It is the equivalent to the Fourier transform in a plane but on a sphere. Since the diffusion is real and symmetric, a truncated version of the SH can be used, only including real and even components. The first harmonic orders are visualized in Figure 2.9. The diffusion signal can be estimated using a truncated SH series of order l_{max} with $(l_{max}+1)(l_{max}+2)/2$ coefficients. For example, the WM response function can be modeled using an SH series of order $l_{max} = 8$, which has 45 SH coefficients.

CSD has been extensively used for WM investigations, especially in studies based on tractography since it is quite successful in extracting crossing fiber directions. An extension to CSD is MT-CSD, which adds different tissue compartments

to the model, accounting for signal differences in WM, GM and CSF. MT-CSD is the main method used in this thesis and will therefore be described in more detail in the next section.

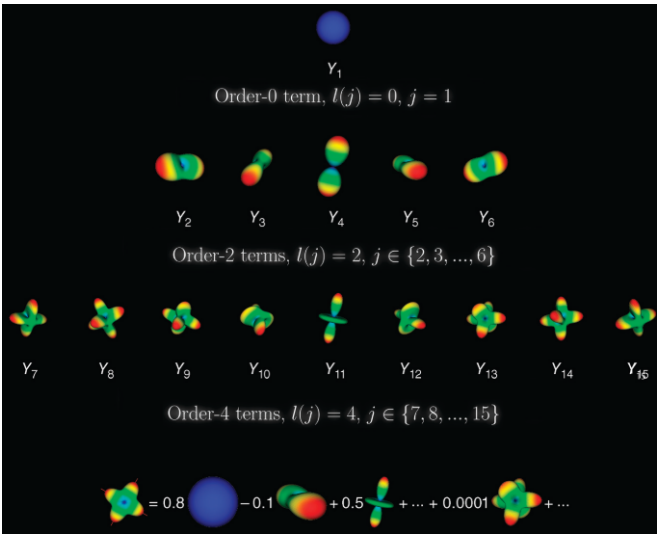

Figure 2.9 Spherical harmonic basis. Visualization of the first elements of the modified SH for representation of diffusion signal. Each signal can be decomposed into a sum of SH, as illustrated at the bottom. Image from [18].

Multi-tissue Constrained Spherical Deconvolution

MT-CSD [32] is an extension of CSD, taking into account different tissue types (WM, GM, CSF) and their corresponding response functions. MT-CSD can produce volume fraction maps of the tissues and therefore also a segmentation into WM, GM and CSF solely based on the diffusion signal. An example of this can be seen in Figure 2.10. By accounting for GM and CSF fractions, MT-CSD achieves better results in fiber reconstruction than CSD, which is its main application. However, recent studies also successfully used the tissue fractions as metrics, giving some more insight into changes in microstructure [43, 33]. In this thesis, MT-CSD will be the main method used to extract different metrics (for more details see Chapter 4). MT-CSD works with single-shell and multi-shell acquisition, i.e. acquiring MRI images with one (and b=0) or several b-values. In this thesis, multi-shell images are used and therefore multi-shell MT-CSD.

The model assumes three compartments, that correspond to the WM, GM and CSF[3]. The WM compartment is modeled as anisotropic, while GM and CSF are

[3] the model could be extended to an arbitrary number of compartments

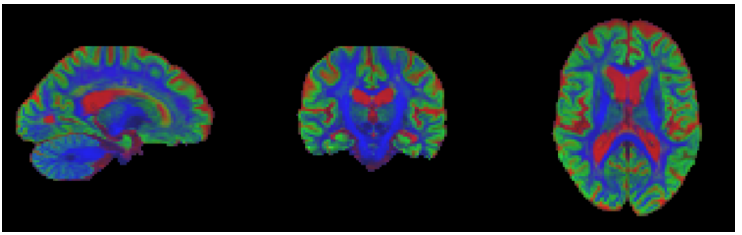

Figure 2.10 Segmentation of the brain based on diffusion signal by MT-CSD. Green: GM, Red: CSF, Blue: WM.

modeled as isotropic. This is achieved by estimating the WM response function as an SH series of order $l_{max} = 8$ with 45 coefficients, while GM and CSF responses are estimated by an SH series of order 0 with only 1 coefficient. Each of the response functions is estimated directly from the diffusion signal, by selecting voxels of high WM/GM/CSF content and fitting the SH series to the averaged signal of these voxels. This process has been optimized over the last years. For more details on the selection of the voxels and the response function estimation, the reader is referred to [32, 21, 20]. By basing the response functions solely on the recorded data, every microstructural property is captured by it. This is one of the advantages over a biological-based model, since there is no need to consider every cell type or structure that might be present in WM or GM. This makes this method usable without imposing any assumptions, but also makes it harder to interpret, since it is not clear what structural changes cause differences.

For each b-value, the unique response of each tissue is estimated. The GM and CSF responses are modeled as spheres, reducing in size with higher b-values (as the signal decreases with higher b-values). The WM response can be represented by a sphere at b=0 (no diffusion encoding) but has a distinct shape for higher b-values (see Figure 2.11 bottom). When plotting the response function depending on the b-value, the different tissues exhibit different behavior (see Figure 2.11 top), which is caused by differences in diffusion based on differences in the microstructure.

By leveraging the different response functions, MT-CSD is able to separate the signal into the three compartments leading to three separate tissue maps. While the GM and CSF tissue maps are scalar, representing the volume fraction, the WM tissue maps are composed of 45 maps, representing the SH coefficients. From these tissue maps, a contribution map can be retrieved, showing a segmentation into GM, WM and CSF (see Figure 2.10). The segmentation achieved by MT-CSD is comparable to a segmentation based on structural images [32]. Fraction maps can be formed by normalizing the tissue maps (with the first slice of the WM tissue map, corresponding to the b=0 acquisition), giving the relative volume fraction of each tissue in each voxel.

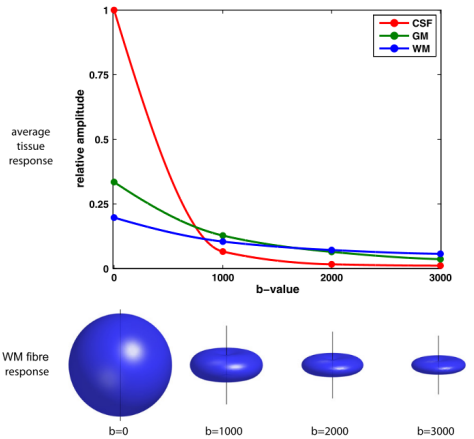

Figure 2.11 Typical response functions for the three compartments in MT-CSD. WM fiber responses are visualized at the bottom, dependent on the b-value. GM and CSF response functions are left out as they are just modeled by spheres decreasing in size with higher b-values. Image from [32].

2.6 Statistical Evaluation

There are two main approaches when it comes to group-based comparisons of MRI data, region-based and voxel-based. For comparing regions of interest (ROI) a predefined set of labeled regions (called atlas) is applied to the parametric map and summary values (usually the mean or the median) of the metric of interest are extracted for each region. The voxel-based approach compares, as the name suggests, metrics per voxel, meaning that the same voxel in each subject's scan is compared across all subjects. For this approach, the images need to be registered to a common space to enable the comparison of the same voxel across subjects.

In this thesis, two different processing pipelines are used for the voxel-wise comparison, voxel-based morphometry (VBM) [6] and GBSS [9]. The GBSS steps prior to the statistical analysts are also used for a region-based analysis. Both approaches are described in more detail below.

Voxel-based Morphometry

VBM is an automated technique that performs a voxel-wise comparison between groups to identify differences between groups. VBM can identify local differences across subjects and is often used for GM comparisons. This method is used in many studies and has shown biologically plausible results [75]. VBM can be applied to a wide range of anatomical attributes, like GM density, and analyze them in a simple and unbiased way [5]. It relies on spatial normalization and smoothing, which removes any large-scale anatomical differences. The main steps of VBM are shown

in Figure 2.12, based on [6, 5, 75]. A more detailed description of the steps is given in Chapter 4.

Figure 2.12 Steps of VBM.

The interpretation of the statistical analysis remains a challenge. Differences can be explained by multiple circumstances, e.g. thinning or thickening of the cortex, different folding, and also misregistration of images [5].

VBM is criticized for some problems, like the effects of misalignment, partial volume effects and differences in kernel size (for smoothing) which make it hard to compare studies [75]. To overcome some of these problems, another voxel-based methodology was introduced: GBSS.

Gray Matter based Spatial Statistics

GBSS is a method used to perform a voxel-wise comparison of GM microstructure. It is based on tract-based spatial statistics [61], a popular method to perform statistical analysis on WM. GBSS works by skeletonizing the GM and projecting the metric of interest onto the skeleton. It was first introduced by Ball et al. (2013) [9] and then altered by Nazeri et al. (2015) [44]. The main steps of GBSS are shown in Figure 2.13 and are described in the following based on [44]. The segmentation and skeletonization process was altered in this thesis and is described in the method section (Chapter 4) in more detail.

Figure 2.13 Steps of GBSS.

In the original GBSS pipeline [44], the GM maps were calculated by subtracting the WM fraction (derived from FA maps) and the CSF fraction (estimated using NODDI [77]) from 1 (see Figure 2.14). In this thesis, the GM fraction will be estimated directly from the diffusion signal using MT-CSD.

Once all GM maps (and other maps of interest) are registered to the same space, the GM is skeletonized by only keeping voxels with a GM fraction $f_{GM} > 0.7$ in >75% (values were varied here) of the subjects. The metrics of interest are then

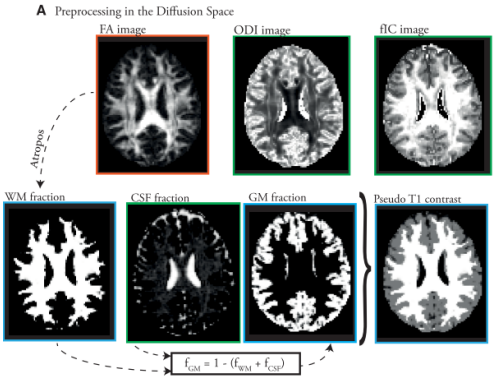

Figure 2.14 The estimation of GM fraction maps for GBSS as described by [44]. Image from [44].

projected onto the skeleton by searching perpendicular to the skeleton for the most probable GM voxel and using that value for the skeleton. This process is done for every voxel of the skeleton in every subject, ensuring that the comparison across subjects is done on only GM voxels. This minimizes the partial-volume effect as well as the effects of slight misregistrations.

3

Motivation

This chapter aims to give a brief overview of the current research in dMRI based biomarkers for AD to set this work into context and provide some motivation for it.

3.1 Current Biomarkers

The most commonly used MRI biomarker in clinical studies on AD is cortical thickness (CTh), e.g. [42, 62]. CTh is used to capture cortical thinning and atrophy. Several studies have shown reduced CTh in areas that align with typical patterns of disease progression [12]. Atrophy is first observed in the entorhinal cortex and hippocampus [23], in later stages the whole medial temporal lobe is affected [40]. However, microstructural changes are thought to appear years before atrophy becomes apparent. One method with the potential to capture microstructural changes is dMRI. A few biomarkers based on dMRI seem promising, including MD based on DTI [38] and metrics based on NODDI [77].

Several studies show elevated MD in cortical areas that correspond with areas affected by atrophy [56, 63]. There is some controversy if MD is independent of CTh and if it is more sensitive for early detection of AD. Some studies [57, 74] reported that MD is independent of CTh and give a better prediction of disease progression. On the other hand, it has also been reported that the effect size of CTh remains equal to or even better than MD concerning differentiation between disease stages [14].

Another recently studied biomarker is the neurite density index and the orientation dispersion index based on the NODDI model [77]. Studies have shown that these metrics provide additional information compared to cortical thickness and show differences before atrophy becomes apparent [51, 72]. The neurite density index reduces in areas that are early affected by Aβ, which makes it a promising early biomarker [72]. However, NODDI has been criticized for invalid assumptions, especially in the pathological case.

Even though the dMRI based biomarkers seem promising, cortical thickness is still the most commonly used biomarker in clinical studies. The proposed metrics have some drawbacks, especially the interpretation is very challenging. However, a dMRI based biomarker capturing microstructural changes could potentially be

very useful to gain a deeper understanding of the disease progression. This thesis aims to investigate the potential of MT-CSD based metrics as biomarkers. MT-CSD is a signal based model, which does not impose any biological assumptions like NODDI. By modelling the different tissue fractions it might also be less sensitive to partial volume effects than MD.

3.2 Use of MT-CSD and GBSS

While MT-CSD is mainly used for investigations of the WM, a few studies have started using the GM and CSF fraction as metrics to investigate changes in GM [33] or pathological changes in WM [43]. Jillings et al. [33] studied macro- and microstructural changes in the brains of astronauts after returning from space. By using GM-, WM- and CSF-fraction they showed morphological changes of the GM, which was not observed to this extent before. Mito et al. [43] used the tissue fractions to investigate and classify WM hyperintensities in AD patients. They showed that WM hyperintensities exhibited distinct tissue profiles and concluded that it can be beneficial to use microstructural information (i.e. MT-CSD metrics) for the classification of WM hyperintensities. These two examples show the potential of these metrics and how they can add valuable information. To the best of my knowledge, MT-CSD has not been used to study pathological changes caused by AD in GM yet.

GBSS was first introduced by Ball et al. [9] to study the development of cortical microstructure in the brain. It has been modified by Nazeri et al. to study changes in the GM across the human lifespan [44] and GM microstructure changes in neurological disorders [45]. A recent study by Vogt et al. [72] uses GBSS to investigate GM changes in AD, comparing NODDI metrics with CTh. All these studies have shown plausible results with the GBSS pipeline in very similar applications to this thesis. Therefore, the GBSS pipeline was chosen to investigate the potential of MT-CSD metrics.

4

Methods

This chapter covers the used methods and explains the constructed pipeline in detail.

4.1 Data

The data used in this thesis is part of the Swedish BioFinder2 study[1]. The aim of this study amongst others is to develop methods for the diagnosis of AD and Parkinson's disease and examine the underlying mechanisms. The study includes over 1600 subjects (with Parkinson's disease, Alzheimer's disease and healthy subjects) that undergo repeated examinations that include amongst others MRI scans and Aβ and tau PET scans.

For this thesis, the dMRI scans of 200 subjects (100 healthy controls, 100 on the AD spectrum) were used. The participants were classified as A-T- (n=100), A+T- (n=50) and A+T+ (n=50) according to Aβ and tau PET uptake, based on previously published thresholds [39, 48]. For example, participants with low Aβ (A-) and low tau (T-) values make up the healthy control group A-T-. An overview of the participants is given in Table 4.1. The aim was to study microstructural differences that appear in different stages of AD, defined by the uptake of Aβ (A) and tau (T). Therefore, A+T- and A+T+ were compared to the healthy controls A-T-. From each participant only one time-point (i.e. one scan) is included, making this a cross-sectional study, meaning that only differences between the groups can be investigated but not direct changes with the progression of AD.

Group	# of subjects	Avg. Age	Sex (f/m)
Healthy Controls (A-T-)	100	66.3 ± 9.5	51/49
Aβ+/Tau- (A+T-)	50	70.7 ± 8.6	25/25
Aβ+/Tau+ (A+T+)	50	71.7 ± 6.7	26/24

Table 4.1 Overview of subjects included in the analysis.

[1] `https://biofinder.se/`

MRI scans were performed on a MAGNETOM Prisma 3T scanner (Siemens Healthcare, Erlangen, Germany), equipped with a 64-channel head coil. A single-shot echo-planar imaging sequence was used to acquire 104 diffusion-weighted volumes (repetition time: 3500 ms; echo time: 73 ms; resolution: 2x2x2 mm^3; field of view 220x220x124 mm^3; b values range: 0, 100, 1000, and 2500 $\frac{s}{mm^2}$ distributed over 2, 6, 32, and 64 directions; twofold parallel acceleration and partial Fourier factor=7/8).

4.2 Software

The main softwares used are MRtrix3 [65], FSL [60] and ANTs [7] for the processing and statistical analysis of the images and Matlab for simulations. The pipeline was partly implemented in nipype [26] and partly as bash scripts (run on Ubuntu 20.02). MRtrix3, FSL and ANTs are advanced software packages for MRI processing, nipype is a framework in python that provides wrappers for many common functions from these software packages, enabling the combination of them in one script.

The main functions used are listed in Table 4.2. Note that not all functions used in this thesis are listed here, only functions for the main steps of the pipeline. The function of each command will be described in detail in the pipeline section.

part of pipeline	**command**	**software**	**based on**
preprocessing	dwidenoise	MRtrix3.0	[69]
	mrdegibbs	MRtrix3.0	[36]
	topup	FSL v6.0	[2]
	eddy	FSL v6.0	[1, 3]
	dwibiascorrect	MRtrix3.0	[67]
model-fitting	dwi2response	MRtrix3.0	[21, 20]
	dwi2fod	MRtrix3.0	[32]
	dtifit	FSL v6.0	
template building	antsMultivariateTemplate-Construction2.sh	ANTs v2.3	[8]
registration	antsRegistration	ANTs v2.3	
	antsApplyTransforms	ANTs v2.3	
statistical evaluation	tbss_skeleton	FSL v6.0	[61]
	randomise	FSL v6.0	[76]

Table 4.2 Main functions used in the pipeline.

4.3 Pipeline

The processing pipeline consists of four main steps: the preprocessing of the images, the extraction of different model parameters of the diffusion images, the alignment of the images to a template and the statistical evaluation. The first two steps are implemented in nipype, allowing for parallel execution of the preprocessing steps. The other steps are executed as bash scripts. An overview of the whole pipeline can be seen in Figure 4.1 and its steps being explained in detail in the following.

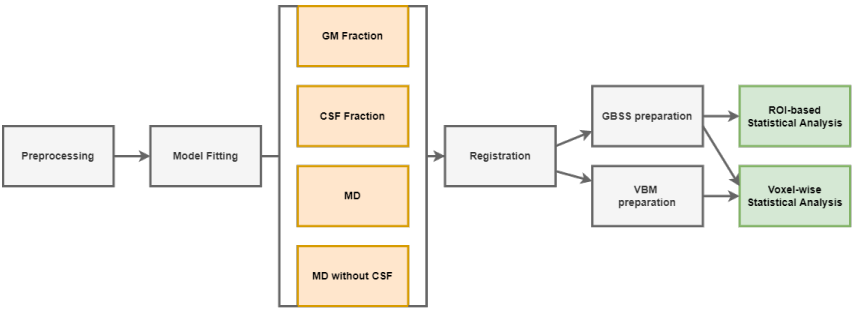

Figure 4.1 Overview of the pipeline.

Preprocessing

The steps of the preprocessing were chosen based on previous publications that used MT-CSD [33, 31, 43]. The implementation of the preprocessing was based on an existing preprocessing pipeline, consisting of suspectibility-induced distortion, motion and eddy correction. In this thesis, additional preprocessing steps (denoising, Gibbs removal and bias field correction) were added to it. An overview of the preprocessing steps is given in Figure 4.2.

The dMRI images were corrected for several known artifacts[2] to improve the quality and the following analysis. First, denois using random matrix theory [69] was applied. Next, the Gibbs ringing artifact removal based on local subvoxel shifts [36] was applied. Then, susceptibility-induced distortions were estimated using reversed phase-encoded images [2] and corrected for. Subject motion and eddy current induced distortion were also corrected using the method described in [1, 3]. Last, the bias field (intensity inhomogeneity) was estimated and corrected [67]. The whole preprocessing pipeline is implemented in nipype and takes 24-48 hours to run for all subjects, depending on the computer. This step was the most time-intensive one in the whole pipeline.

[2] Each artifact and its correction is described in more detail in the appendix.

Before continuing with the next steps, all 3D volumes were visually inspected to ensure a successful preprocessing. Two subjects had to be replaced by other subjects (same group, age and gender).

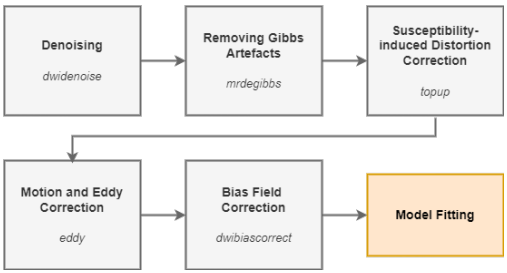

Figure 4.2 Overview of the preprocessing steps and the used functions.

Model fitting

From the preprocessed images, five metrics on the GM were extracted, using two different models: DTI and MT-CSD. From DTI, MD maps of the preprocessed image and of a CSF-regressed image (using MT-CSD) were derived. From MT-CSD, GM-/WM- and CSF-fraction maps were extracted. These maps were used as metrics directly and as tools for masking the image, building the skeleton and for CSF-regression. The study-wise template and registration of images were also based on the GM fraction maps.

MT-CSD The main part of the thesis focuses on the MT-CSD model. First, the response functions for the three tissues (GM, WM, CSF) were calculated. This can be done either individually for every subject or by using a group-averaged response function. Since the latter was used in several relevant previous studies [33, 31, 43], this option was chosen for this work as well. The group averaged response function was based on 42 representative subjects (21 A-T- (avg 70.5 years), 21 A+T-/+ (avg 70.1 years)). These 42 subjects were also used to build the study-specific template. The group-averaged response functions were then used as input to the MT-CSD algorithm for every subject, that outputs the tissue maps. The outputted tissue maps have relative values, so to enable intra-subject comparisons the tissue maps were normalized to 1, i.e. the sum of the GM, WM and CSF tissue maps is 1 in every voxel. These normalized maps are referred to as tissue fraction maps and are used for all following steps (except for the CSF regression, where the relative tissue maps are used). An overview of the MT-CSD step is given in Figure 4.3. The whole process for MT-CSD is implemented in nipype, this step takes approximately 3 minutes per subject.

All tissue fraction maps were visually inspected and no images had to be excluded in this step. An example of the tissue maps can be seen in Figure 4.4

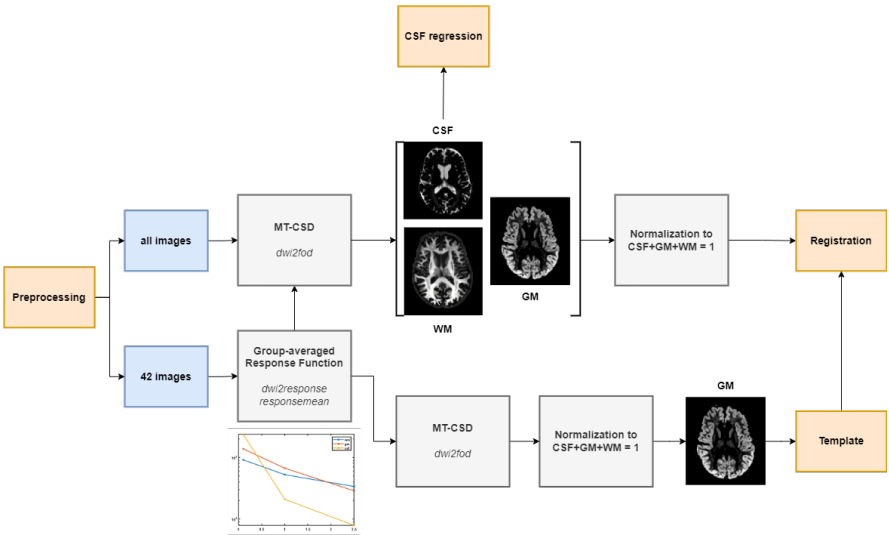

Figure 4.3 Overview of the MT-CSD model fitting. 42 images are used for the average response function and the study-wise template. For the analysis, average response functions are used as input for the MT-CSD algorithm. For the next steps, all tissue maps are normalized so the fractions of WM, GM and CSF sum up to 1.

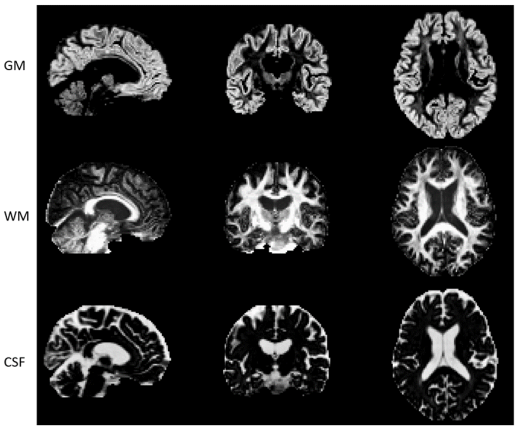

Figure 4.4 Tissue fraction maps of one subject.

CSF regression If a voxel consists of both GM and CSF so-called partial volume effects can occur. In CSF the diffusivity is higher than in GM. So, in voxels with a higher CSF fraction, the MD will also be higher. This can confound the GM diffusivity, which is the actual metric of interest. In this thesis, a new method[3] to remove the CSF signal was tested.

The idea is to suppress signal caused by CSF to minimize partial volume effects and capture the "true" diffusivity of the GM. First, the CSF tissue map was obtained with the MT-CSD model (as described above). Then, the process was reversed by predicting the diffusion signal caused by the CSF by spherical convolution of the CSF tissue map and its response function (using *shconv* and *sh2amp* from MRtrix3.0). Lastly, the predicted CSF signal is eliminated from the preprocessed image and the MD map is calculated from the CSF-regressed image. This MD map is referred to as MD_{nocsf} in the following. In Figure 4.5 the process is visualized and in Figure 4.6 one example of this regression and the resulting MD map can be seen.

It has to be noted, that in some cases the CSF regression leads to an unstable DTI fit in areas where no signal is left. This is visible in the ventricles and CSF outside the brain. This is however not too concerning, as only the cortex is investigated in this thesis. The cortex should not affected by this problem, as the GM signal is usually high in this part of the brain.

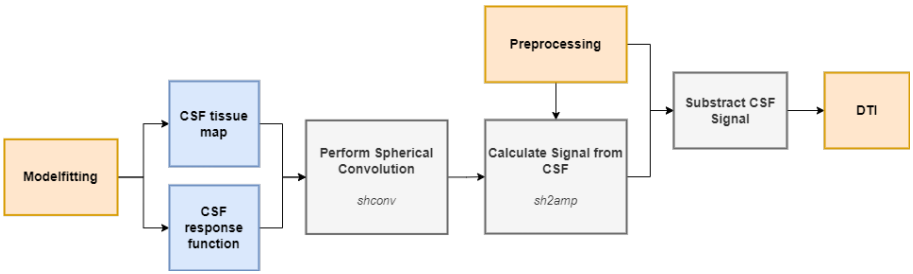

Figure 4.5 CSF regression of preprocessed images. Note that the unnormalized CSF tissue map is used for the estimate of the CSF signal in the original preprocessed image. MD maps are calculated for CSF-regressed images. *Add images*

DTI The MD maps were calculated using the command *dtifit* in FSL. This fits the tensor model to the data and gives amongst other the MD and FA maps as output. As input, the preprocessed images as well as the CSF-regressed image and a corresponding brain mask (computed with *dwi2mask* in MRtrix3.0) were used. This step was implemented in nipype as well.

[3] based on a forum discussion
`https://community.mrtrix.org/t/free-water-compartment-analysis`

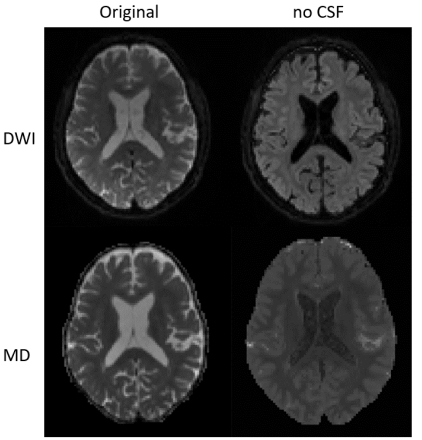

Figure 4.6 Example of CSF regression. The top row shows the diffusion-weighted image with and without CSF signal and the bottom row shows the corresponding MD map.

Template Building and Registration

For the statistical analysis using GBSS or VBM, all the images need to be aligned in a common space. This can be done using linear and non-linear registration of the image to a template, which defines a common space to which all images are aligned. The template can either be a standard template or a study-wise template, i.e. the average of all subjects or a subset of subjects. Once an image is registered to the template, other images (e.g. tissue maps, MD maps) from the same subject (and in the same space) can be aligned with the template by applying the same transformation.

Template One option for the template would be to use an existing standard template. Most standard templates are however based on T1w images and not necessarily suited for diffusion images as used in this thesis. Therefore, the template was based on the GM fraction maps of the same 42 subjects as used for the group-averaged response function. To ensure a good template, the 42 subjects were inspected carefully. Only subjects with full brain scans and not too enlarged ventricles were included in the template. The template was built using the *antsMultivariateTemplateConstruction2.sh* script from ANTs (4 (+4) iterations, using rigid, affine and non-linear registration with greedy SyN model). The final template is shown in Figure 4.7. This was the most time-intensive step after the preprocessing and takes around 12 hours to run on CPU, or 5-6 hours using GPU.

Registration After the template was created, the GM fraction maps of all subjects were registered to the template. The registration was executed using *antsRegistra-*

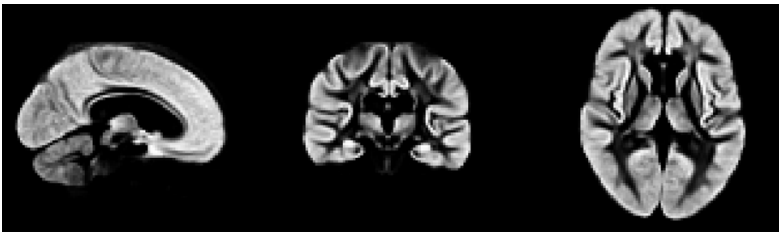

Figure 4.7 Study specific template based on GM fraction maps.

tion. The registration includes three stages: rigid, affine and non-linear (B-spline Syn) transformation. The registration step outputs the affine transformation matrix and the non-linear warp field as well as the aligned GM fraction map. The registration for all 200 GM fraction maps takes around 6 hours to run on CPU.

Using the affine transformation matrix and the non-linear warp field the remaining tissue fraction maps and the MD and MD_{nocsf} maps were aligned to template space using the command *antsApplyTransforms*.

After registration and transformation, all images were visually inspected to ensure a correct alignment. One subject (A-T-) had to be excluded at this step, as the registration failed to align the GM fraction map with the template.

Alternative Template An alternative template based on pseudoT1 volumes was considered, as it is done in previous publications using GBSS [44, 45, 72]. The pseudoT1 volume was constructed by adding the WM fraction map and the GM fraction map (weighted with a factor of 2 to get a T1w-typical contrast between GM and WM). An example of the pseudoT1 image and the pseudoT1-based template is shown in Figure 4.8. Based on visual inspection of the templates and the resulting registration routine, the template based on the GM maps was chosen. The pseudoT1 template showed slightly worse alignment and it resulted in four failed registrations in contrast to one with the GM fraction template.

GBSS

The main statistical analysis is based on GBSS. For GBSS the GM is skeletonized and all metrics of interest are projected onto the skeleton, which can then be used for the statistical analysis. For this, the aligned GM fraction maps were first merged and averaged. Based on the average of all subjects, the GM skeleton was then produced by running *tbss_skeleton* with a threshold of $f_{Gm} > 0.55$ (based on [52]). Next, all metrics (MD, MD_{nocsf}, WM-fraction, CSF-fraction) were projected onto the skeleton[4], which is done by searching for the most probable GM-voxel perpendicular to the skeleton and using the value (of the metric of interest) of that voxel. This step results in a 4D-image for each metric consisting of the skeleton with the projected

[4] based on the implementation of Nazeri et al. [44]

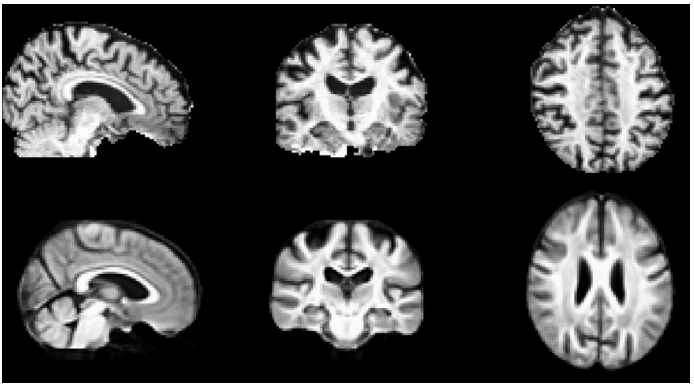

Figure 4.8 PseudoT1 image example (top) and template (bottom).

metrics for all subjects. These files are used for the voxel-wise and region-based statistical analysis in the next step. For the region-based analysis, an atlas (Desikan-Killiany atlas [19]) was registered to template space and the skeleton was matched to the cortical regions.

Separate skeletons and 4D files were produced for both group-wise comparisons (between A-T- and A+T- or A+T+ respectively). The skeletons only differ in very few voxels, the 4D files consist only of the subject included in the respective groups.

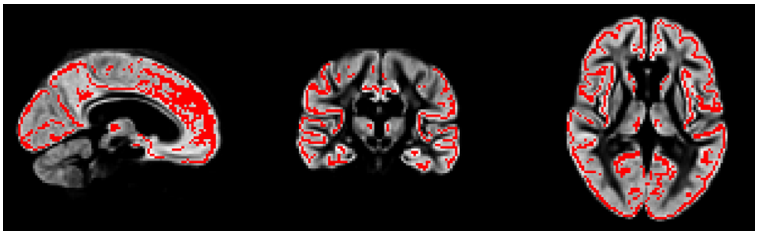

Figure 4.9 GM skeleton (red) on the GM template.

VBM

For comparison, a voxel-wise analysis based on VBM was performed. For the VBM analysis, the aligned maps were corrected for volume change during the registration step and smoothed. The correction for volume change was done by multiplying the image with the Jacobian determinant of the wrap field, which was calculated using *ANTSJacobian*. The images were smoothed using a a Gaussian kernel of size 3mm. Finally, all GM maps were merged into a 4D file for the statistical analysis. Only

GM fraction maps were used for a VBM analysis, all other metrics were only used in the GBSS pipeline.

4.4 Statistical Evaluation

The group-wise statistical analysis was performed both voxel-wise and region-based for two comparisons: A-T- (healthy) and A+T-, and A-T- and A+T+. All comparisons were corrected for age and sex. This enables an investigation of microstructural changes that occur with the presence of Aβ and tau. For the voxel-wise analysis of the GM-fraction, the GBSS and VBM pipeline were used while all other metrics (CSF- and WM-fraction, MD, MD_{nocsf}) were only compared using the GBSS pipeline. A region-based analysis for GM- and CSF-fraction, MD and MD_{nocsf} was done based on the GBSS pipeline with the use of the Desikan-Killiany atlas [19]. For comparison, the region-based analysis for cortical thickness was done using the software FreeSurfer[5].

Voxel-based analysis

For the voxel-based analysis, the 4D files created by the GBSS and VBM pipeline were used. A non-parametric voxelwise analysis was performed using *randomise* with 5000 permutations while controlling for age and gender. Threshold-free cluster enhancement was used [59] and the results are corrected for family-wise error (FWE) due to multiple comparisons. A p-value of $P_{FWE} < 0.05$ is considered significant. Each group-wise comparison was performed twice to test the two hypotheses A-T- < A+T-/+ and A-T- > A+T-/+.

Region-based analysis

For the region-based analysis, the median value of each metric in every region (defined by the atlas) was extracted from the skeleton of all subjects. For further analysis regions relevant to AD pathology were chosen (see Table 4.3). This regions are affected early by Aβ (earlyAb ROI) or correspond to regions affected during the Braak-stages I-IV (temporal ROI) [11]. For both regions the mean value of all included ROIs weighted by their size on a subject basis was used for the following statistical analysis .

For both regions, a statistical analysis was performed using a t-test as well as ordinary least squares regression with age and gender as confounders. Again, two group comparisons were performed: A-T- and A+T-, and A-T- and A+T+. Addi-

[5] `https://surfer.nmr.mgh.harvard.edu`

	ROIs
EarlyAb ROI	isthmuscingulate, lateralorbitofrontal, medialorbitofrontal, posteriorcingulate, precuneus, insula
Temporal ROI	entorhinal, fusiform, inferiortemporal, middletemporal, parahippocampal

Table 4.3 ROIs included in the EarlyAb ROI and Temporal ROI. For all ROIs the left and right regions in the brain are included, all are cortical ROIs based on the Desikan-Killiany atlas [19].

tionally, the effect size for each metric was calculated, using Cohen's d [15]:

$$d = \frac{\mu_1 - \mu_2}{s} \tag{4.1}$$

$$s = \sqrt{\frac{(n_1 - 1)s_1^2 + (n_2 - 1)s_2^2}{n_1 + n_2 - 2}} \tag{4.2}$$

where μ is the mean of each group, $s_{1,2}$ the standard deviation and $n_{1,2}$ the sample number. The effect size is a quantitative measure, which indicates how large the difference between two groups is. The exact interpretation of the effect size however depends on the use case. Generally, effect sizes below 0.3 are considered small and above 0.8 are considered large [15].

For comparison and validation of the implemented pipeline, the median values for each ROI were also extracted using an already existing pipeline using FreeSurfer[6]. This pipeline segments the cortex based on the T1 image and extracts the regional median values. This was done for GM-fraction, MD and MD_{nocsf}. The cortical thickness was also extracted to compare the results to the golden standard metric.

4.5 Simulation

To gain a deeper understanding of what causes changes in the tissue fractions, simulations in Matlab were done. For this, several simulations were designed, investigating how the estimated fractions change if the tissue fractions in a voxel change or the apparent diffusivity of GM changes.

Using an open-source framework for the analysis of dMRI data in Matlab [46], dMRI signal stemming from WM, GM and CSF was simulated. The parameters for the simulation were adjusted so the resulting signal matches the mean response functions of the tissues acquired from the data. The response functions of that the simulated data and the response functions acquired from the data are similar, as it

[6] This part was not implemented by myself and is therefore not described in this thesis, only the values were used for the statistical analysis.

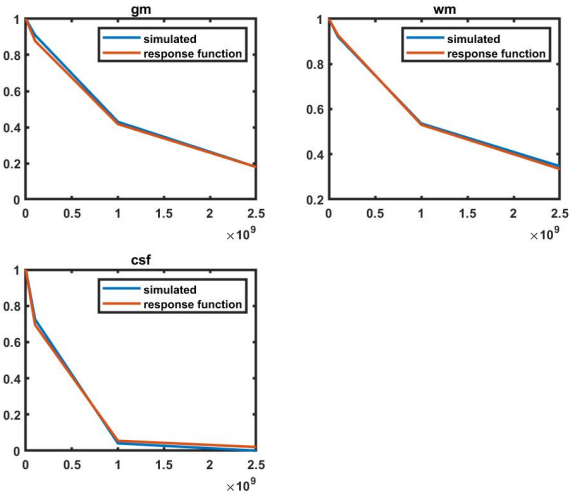

Figure 4.10 Response function of the simulated tissue signal and the response functions based on the data.

can be seen in Figure 4.10. The final parameters are as follows: WM is simulated with an axial diffusivity of $2.6\frac{mm^2}{s}$ and radial diffusivity of $0.3\frac{mm^2}{s}$, GM with a diffusivity of $0.95\frac{mm^2}{s}$ and CSF with a diffusivity of $3.2\frac{mm^2}{s}$.

Three simulations were designed, two with varying the GM-fraction and the WM- or CSF-fraction and one altering the diffusivity of GM. For all simulations a 100x100x3 volume was simulated, with the voxels on the diagonal containing signal composed of simulated GM, WM and CSF signal in varying fractions or GM signal with varying GM diffusivity. For the first simulation, the simulated signal was composed of GM and WM signal, varying the fraction of GM from 100-0% and the WM fraction from 0-100% accordingly. The second simulation was very similar, just with CSF signal instead of WM signal. The goal of these two simulations was to give a deeper understanding how the estimated tissue fractions change if the real (or in this case simulated) tissue fractions change. The third simulation aimed to investigate the behavior of the model if the diffusivity of GM changes, which is expected in pathological cases. This simulation was done with 100% GM signal with varied diffusivity between $0.5\frac{mm^2}{s} - 1.5\frac{mm^2}{s}$.

5

Results

This chapter gives an overview of the results of the group comparisons. The comparisons were done in a voxel-wise and a region-based analysis. To visualize results better, the software *SurfIce*[1] was used to project the statistical maps onto a standard brain surface. A discussion and interpretation of the results can be found in Chapter 6.

5.1 Voxel-wise Analysis

GBSS

GBSS was used to investigate differences in GM/CSF/WM fraction and MD (with and without correction for CSF) between the A-T- group and both A+T- and A+T+ in pairwise comparisons. For both groups, a lower GM fraction and a higher CSF fraction were observed compared to A-T-. The A+T+ group displayed more significant differences than the A+T- group. In A+T- the GM fraction was lower than in A-T- mainly on the left frontal and temporal regions (see Figure 5.1 left), in A+T+ the lower GM fraction was more widespread over the brain (see Figure 5.1 right). A similar pattern can be observed for the CSF fraction (see Figure 5.2), which showed a higher value for both groups compared to A-T-. The differences for A+T- were mostly restricted to the frontal lobe (see Figure 5.2 left) but widespread for A+T+ (see Figure 5.2 right). Significant WM fraction changes were only observed for A+T+, which showed a higher WM fraction mainly in the frontal and temporal lobe (see Figure 5.3).

For MD significant changes were observed for A+T+, but not for A+T-. MD was higher over the whole brain (see Figure 5.4 left). When correcting MD for CSF, the differences disappeared in A+T+ and lead to a decrease in MD in the frontal regions for A+T- (see Figure 5.4 right).

All changes are summarized in Table 5.1. Additional visualizations of the results are given in the Appendix in Figures B.1, B.2, B.3.

Note that the top part of the brain was not included in the skeleton, therefore differences in these areas were not detectable.

[1] `https://www.nitrc.org/projects/surfice/`

	GM fraction	CSF fraction	WM fraction	MD	MD_{nocsf}
A+T-	↓ f t	↑ f	-	-	↓ f
A+T+	↓ w	↑ w	↑ f t	↑ w	-

Table 5.1 Overview of significant ($p_{FWE} < 0.05$) differences with respect to A-T- determined with voxel-wise comparison based on GBSS. ↓: decrease, ↑: increase, f: frontal lobe, t: temporal lobe, w: widespread, -: no significant changes.

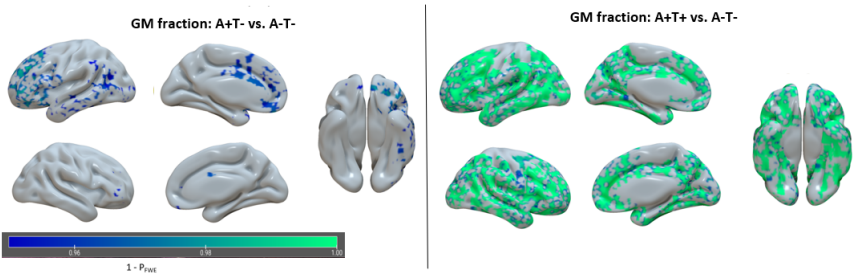

Figure 5.1 GM fraction A-T- vs A+T-/+. For A+T- a decrease can be seen in the frontal and temporal left lobes (left). For A+T+ the decrease is widespread (right). Only significant ($P_{FWE} < 0.05$) differences are shown. The statistical maps were projected onto a surface in *SurfIce*.

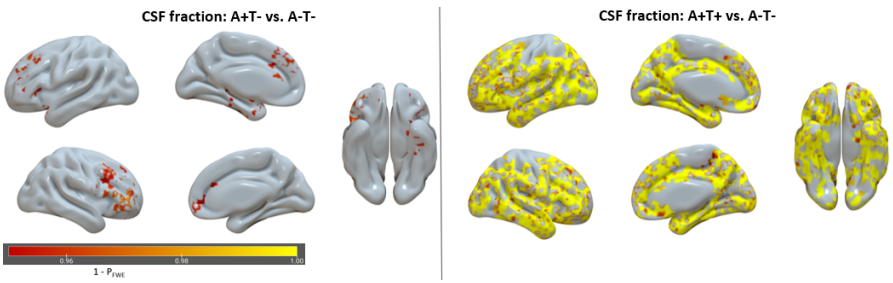

Figure 5.2 CSF fraction A-T- vs A+T-/+. For A+T- only a small increase in the frontal regions is apparent (left), for A+T+ the CSF fraction increased over the whole brain (right). Only significant ($P_{FWE} < 0.05$) differences are shown. The statistical maps were projected onto a surface in *SurfIce*.

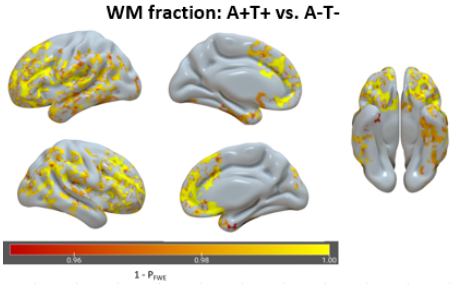

Figure 5.3 WM fraction A-T- vs A+T+. WM fraction increases for A+T+ mainly in the frontal and temporal lobe. For A+T- no significant differences were observed. Only significant ($P_{FWE} < 0.05$) differences are shown. The statistical maps were projected onto a surface in *SurfIce*.

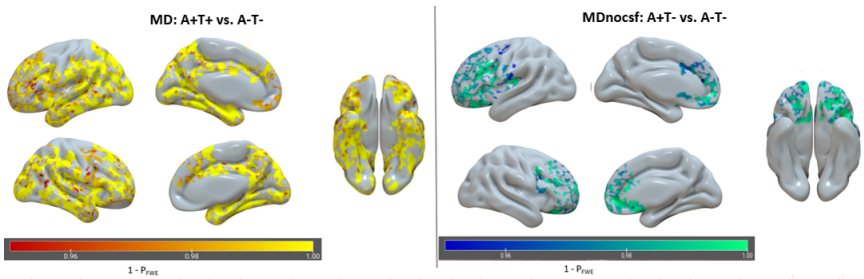

Figure 5.4 MD A-T- vs A+T+ and MD_{nocsf} A-T- vs A+T-. For A+T+ MD increased widespread over the whole brain (left), while no significant differences were observed for A-T- vs A+T-. When correcting for CSF no significant differences for A+T+ remained and for A+T- a decrease in MD was observed in the frontal region (right). Only significant ($P_{FWE} < 0.05$) differences are shown. The statistical maps were projected onto a surface in *SurfIce*.

VBM

The voxel-wise analysis for the GM fraction was also done using VBM. For A+T- no differences were observed compared to A-T-. For A+T+ compared to A-T-, the significant differences are shown in Figure 5.5. The decrease in GM fraction is not as widespread, as observed with GBSS, it focuses mostly on the frontal and temporal lobe. Differences can also be seen in the entorhinal cortex, hippocampus and amygdala, which were also observed with the GBSS pipeline.

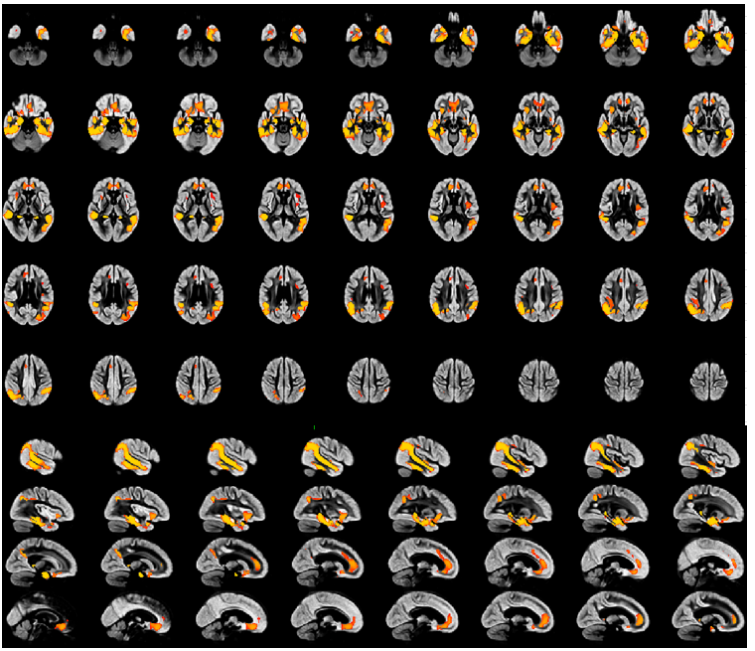

Figure 5.5 GM fraction A-T- vs. A+T+ with VBM analysis. Significant ($P_{FWE} < 0.05$) decreases in GM fraction are shown. Most changes are observed in frontal and temporal regions. For A+T- no significant differences were observed. The statistical map is overlayed on the GM template in *FSLeyes*.

5.2 Region-based analysis

Additionally to the voxel-wise analysis, a region-based analysis was performed. The two regions investigated are the earlyAb ROI and the temporal ROI, these two ROIs consist of several regions that are affected by Aβ early or correspond to cortical regions covered by the Braak stages I-IV [10] respectively. The results are similar to the voxel-wise comparison. The GM fraction was lower in both ROIs for both

groups compared to A-T-, being more prevalent for A+T+. The CSF fraction was higher, again more for A+T+. For MD a higher value was observed for A+T+ in both regions, but not for A+T-. Only for the temporal ROI, a lower value for MD_{nocsf} was observed for A+T-. The distributions of GM/CSF fraction and MD and MD_{nocsf} are shown in Figure 5.6 for the earlyAb ROI and in Figure 5.7 for the temporal ROI.

The significance levels and effect sizes are presented in Table 5.2. The differences in the temporal ROI were larger than in the earlyAb ROI, which also shows in the effect sizes. Significant differences were mainly found for A-T- vs. A+T+, which showed differences in both ROIs and all metrics except for MD_{nocsf}. For the comparison of A+T- with A-T- only one significant difference was found after correcting for age and gender, a lower value for MD_{nocsf} in the temporal ROI.

For comparison, the same analysis was also performed using values generated by the pipeline based on FreeSurfer. The same results were observed, except for MD_{nocsf} being insignificant for both ROIs and groups. Cortical thickness was also analyzed using the FreeSurfer pipeline. It shows a significant decrease in both groups and ROIs with high effect sizes. The highest effect sizes for A+T- vs. A-T- were observed for GM fraction (Cohen's d=0.55 in the earlyAb ROI, Cohen's d=0.6 in the temporal ROI) and CTh (Cohen's d=0.56 in the earlyAb ROI, Cohen's d=0.6 in the temporal ROI) and for A+T+ vs. A-T- in CSF fraction (Cohen's d=1.03 in the earlyAb ROI, Cohen's d=1.39 in the temporal ROI).

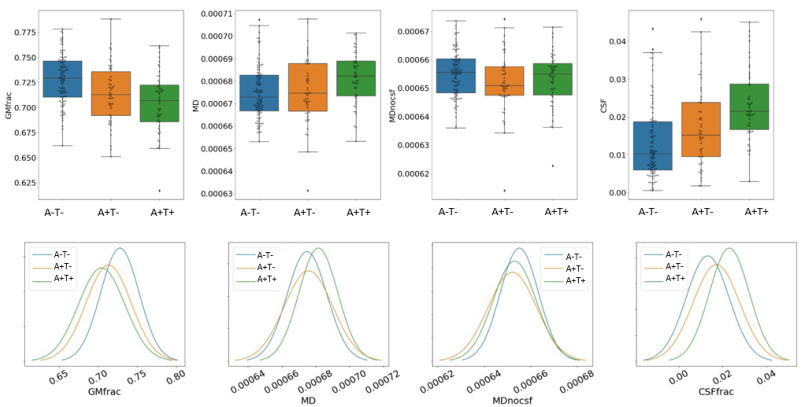

Figure 5.6 Distribution of GM fraction, MD, MD_{nocsf} and CSF fraction in the earlyAb ROI.

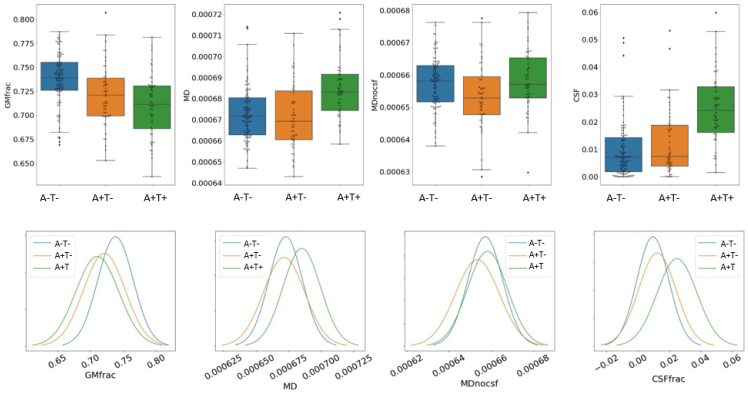

Figure 5.7 Distribution of GM fraction, MD, MD_{nocsf} and CSF fraction in the temporal ROI.

		earlyAb ROI		temporal ROI	
		A+T-	A+T+	A+T-	A+T+
GM fraction	p-value	0.071*	**0.0002**	0.0534*	**5.07E-5**
	effect size	0.55	0.88	*0.60*	0.95
CSF fraction	p-value	0.2852	**7.54E-6**	0.8778	**2.72E-10**
	effect size	0.39	*1.03*	0.25	*1.39*
MD	p-value	0.9714	**0.0106**	0.2309	**2.66E-05**
	effect size	0.07	0.57	0.08	0.92
MD_{nocsf}	p-value	0.2698	0.5197	**0.0462**	0.3766
	effect size	0.33	0.23	0.41	0.11
CTh	p-value	**0.0116**	**1.65E-4**	**0.0114**	**1.68E-10**
	effect size	*0.56*	0.83	*0.60*	1.38

Table 5.2 Summary of the GBSS ROI based statistics (and CTh from a FreeSurfer analysis). p-values are corrected for age and gender, **bold** values are significant ($p<0.05$), values denoted with * are significant when not controlling for age and gender. Effect size calculated with Cohen's d, values in *italic* are the highest effect size for that group and ROI.

5.3 Simulation

Three simulations were designed to gain a deeper understanding of how the tissue fractions react to changes in signal. For the first two simulations, the GM fraction was varied from 0-100% with the rest of the signal being WM or CSF respectively. In the resulting tissue fraction maps, the WM fraction estimated with MT-CSD is higher than it was in the simulated input signal (see Figure 5.8 left). The CSF frac-

tion, however, is underestimated (see Figure 5.8 middle). For example, at simulated GM and WM fractions of 50% each, the GM fraction was estimated at 20% and WM at 78%. For 50% simulated GM and CSF fraction, GM was estimated at 64% and CSF at 36%. The last simulation was 100% GM with varying diffusivity for GM. With lower diffusivity, the WM fraction was rising, while for higher diffusivity the CSF fraction was rising (see Figure 5.8 right). The GM fraction was close to 100% for a diffusivity of 0.9-0.93x$10^{-9}\,\frac{mm^2}{s}$.

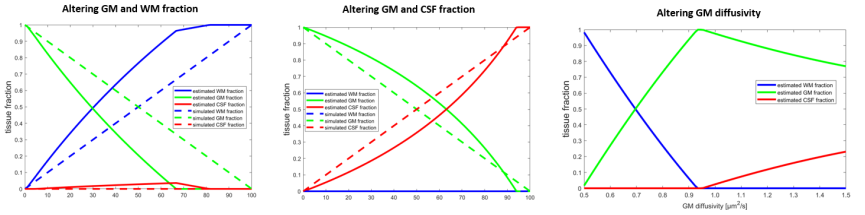

Figure 5.8 Simulation 1 (left): WM fraction 0-100% and GM fraction 100-0% and CSF fraction 0% . An overestimation of WM fraction is visible.
Simulation 2 (middle): CSF fraction 0-100% and GM fraction 100-0% and WM fraction 0%. An underestimation of CSF fraction is visible.
Simulation 3 (right): GM fraction 100% and CSF and WM fraction 0%, the diffusivity of GM is varied between 0.5 and 1.5$x10^{-9}\,\frac{mm^2}{s}$. With lower diffusivity the WM fraction increases, with higher diffusivity the CSF fraction increases.

6

Discussion

The goal of this thesis was to investigate the use of MT-CSD metrics to capture GM microstructure alterations in AD. Tissue fractions (GM, WM and CSF) were compared with MD (with and without correction for CSF) and CTh using voxel-wise and ROI based analysis, based on GBSS. Group differences between groups defined based on evidence of Aβ and tau accumulation (A-T-, A+T-, A+T+) were analyzed.

In the following, the results are critically discussed including an attempt to give explanations for the observed results.

Tissue fractions A reduction in GM fraction with an almost matching increase in CSF fraction can be observed for A+T- and A+T+ in comparison with A-T-. While the differences for A+T- are mostly located in the frontal and temporal lobe, the changes are widespread for A+T+. The reduction of the GM fraction is focused on the frontal lobe, which is an area relatively early affected by Aβ pathology, however no changes are observed in the medial parietal areas, which are also early affected by Aβ [27, 41, 49]. The VBM analysis shows a GM fraction decrease for A+T+ in areas that correlate well with the progression of tau pathology, like the entorhinal cortex, hippocampus and amygdala and the temporal lobe [13, 27, 71].

The increase in CSF fraction is also as expected, since an increase in diffusivity should lead to a higher CSF fraction (as also suggested by the simulations). This is however contrasted by an increase in WM fraction for A+T+ as well, which indicates more anisotropic diffusion or lower diffusivity. This can potentially be caused by inflammatory responses, which could involve microstructural changes, leading to more restricted diffusion.

Overall, the tissue fractions reflect expected microstructural changes. It was to be expected that the differences for A+T+ are more pronounced than for A+T-, as they are further along on the AD spectrum. The tissue fractions show higher significance levels and effect sizes than MD, the current standard metric to measure microstructural changes. Especially for the comparison of A-T- and A+T+, CSF fraction showed high effect sizes (i.e. Cohen's $d > 1$). However, compared to CTh no major improvements are evident. CTh is the only metric that shows significant differences between A-T- and A+T- in the ROI analysis after correcting for age and gender.

Mean Diffusivity As expected from previous studies [56, 74], MD increased in A+T+ compared to A-T-. However, no increase in MD for A+T- was observed. This observation aligns with a study by Rodriguez et al. [55] that also reported an association between MD and tau but not for MD and Aβ.

Even though, the results are as expected, the choice of using GBSS might have influenced the sensitivity towards changes in MD. GBSS is based and tailored towards GM fraction both in the definition of the skeleton and in the selection of the relevant voxel. This approach could bias the analysis selecting the "most" healthy GM voxels i.e., voxels with the highest GM fraction. Moreover, the most sensitive voxel for the analysis of tissue fractions might not be the best candidate for assessing difference in MD.

MD without CSF To reduce possible partial volume effects from the analysis, a new method to eliminate CSF from the signal was developed. These CSF regressed maps were used in a DTI analysis, where MD was extracted (called MD_{nocsf}). The analysis showed no significant differences for MD_{nocsf} for A+T+. One possible explanation would be, that the change in MD was mainly caused by partial volume effects, as also suggested by [29]. However, with GBSS partial volume effects should already be reduced. Therefore, the more plausible explanation is that by trying to regress CSF, small microstructural changes that lead to higher diffusivity were also eliminated, as they would be reflected in a higher CSF fraction. This problem is also discussed in the next section (Interpretation of Tissue Fraction). For A+T-, MD_{nocsf} even decreased compared to A-T-. This effect is in the opposite direction than expected, which indicates the flaws of this method.

VBM vs. GBSS The VBM analysis showed significant differences for GM fraction in plausible areas (corresponding to tau pathology) for the comparison of A-T- and A+T+. However, no significant differences were detected between A-T- and A+T-, whereas GBSS showed differences. Overall, the VBM analysis showed less significant differences in the GM fraction than the GBSS analysis, suggesting that GBSS is more sensitive to group differences. Nevertheless, the results of VBM seem more defined and contained to plausible anatomical regions, thus it remains debatable if GBSS is more sensitive to actual changes or also to false-positive results.

Effect size GM and CSF fraction seem like promising biomarkers as they show high effect sizes similar to CTh (see Table 5.2). However, the metrics should not be judged solely based on the effect size. The effect size does not capture effects of other confounders, which becomes clearer when comparing significance levels as well. For example, for CTh the significance levels are higher than for the GM fraction (especially after correcting for age and gender), even though the effect sizes are very similar.

Simulation The results of the simulation support the observed results. With an increased diffusivity, the CSF fraction is expected to rise according to the simulation. This is exactly what can be observed in the data. In the simulations, an overesti-

mation of WM fraction and an underestimation of CSF fraction (compared to GM fraction) became apparent. According to Jeurissen et al. [32], the overestimation of WM should be mostly eliminated by the use of MT-CSD. So, it remains unclear if this is an actual behavior of the MT-CSD model or caused by deviations in the simulated data from the response functions. If it is caused by the simulated data, this indicates an unstable fit of the model, if the signal from the tissue differs slightly from the estimated response function.

Interpretation of Tissue Fraction

It is important to note that the tissue fractions are hard to interpret and are certainly not equivalent to the exact biological tissue [43]. So for example, a high CSF fraction does not necessarily mean that actual CSF is present in this voxel, only more 'CSF-like' tissue properties, i.e. a higher diffusivity compared to GM. The increase in CSF fraction in the cortex indicates a higher diffusivity, which coincides with the higher MD observed. Equally, a higher WM fraction indicates not actual WM tissue present but more an increase in anisotropic diffusivity.

This leads to a possible problem with the CSF-regression step. As mentioned before, the CSF tissue maps do not necessarily represent CSF, but also 'CSF-like' tissue. When regressing CSF based on the CSF tissue map, not only signal from actual CSF might be eliminated but also any signal stemming from tissue with higher diffusivity. Since the hypothesis is that the diffusivity in GM increases due to cellular changes, it might not be the optimal to remove all signal stemming from 'CSF-like' tissue. This approach should be compared with already established CSF reduction methods in the future, to fully understand its potential and problems.

Another critical point are the group-averaged response functions. The tissue properties might vary across subjects but also within one subject, which could lead to locally different response functions. So, it should be discussed if group-averaged or even global tissue-specific response functions are a reasonable assumption. Considering how much the estimated tissue fractions differed from the 'ground truth' in the simulations, a slightly wrong response function can lead to drastic changes in the tissue fractions. This would make the direct interpretation of the tissue fractions even more complicated.

Pipeline

The main part of this thesis was to build a pipeline using the MT-CSD model. Every part of the pipeline was motivated by interpretation of advantages and potential pitfalls of previous studies. Nonetheless, some changes of the pipeline might be worth considering. The most critical steps are discussed in more detail below.

Preprocessing The preprocessing was based on previous studies using MT-CSD [31, 33, 43]. Since there was a large agreement on the prepocessing steps across these studies, there was no apparent reason to change this. However, the preprocessing took the longest time to complete, so it might be worth considering to drop

some preprocessing steps to save time if it does not impair the results. This would need some extra work to compare the influence of different preprocessing steps on the tissue fractions. Overall, the preprocessing yielded acceptable results (based on visual inspection) and only failed in two cases, which were replaced by two other subjects.

Template and Registration The template building and registration step was one of the most work and time-intensive steps of this thesis.

A bad template can influence the results heavily, especially in voxel-based analysis where the results depend on a good alignment of the anatomical structures. Therefore, several different templates (with subsequent registration) were tested and the best visual result was chosen in the end.

The registration step was modified several times. In the beginning, multiple images didn't align with the template, varied a lot in size or the registration failed. By carefully tuning the parameters of the rigid, affine and non-linear registration and adding a third iteration to every step, the final results aligned well with the template and the skeleton included the major sulci (indentations) of the brain. To visualize this improvement, the mean of all GM fraction maps with the initial and the final registration is shown in Figure 6.1.

However, the registration still could need further improvement and might be an important factor influencing the results. The function used for the registration is normally used for T1w images, which have a higher resolution and contain more anatomical information than the diffusion maps. This might lead to sub-optimal performance when using GM fraction maps as input. The effect of the registration on the skeleton and the results should be investigated in the future and if deemed necessary this step needs to be further improved.

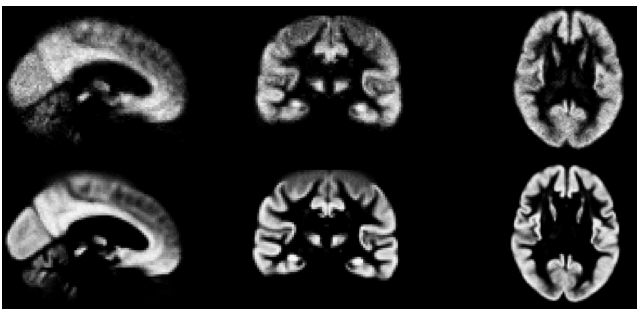

Figure 6.1 The mean GM fraction map across all aligned subjects with the initial registration (top) and the final optimized registration (bottom). A clear improvement is visible. In the final mean more anatomical details can be distinguished.

GBSS This part of the pipeline has the greatest variation from previous studies. Instead of basing the skeleton on NODDI metrics [44] or T1w images [9, 52], the

tissue fraction maps extracted with MT-CSD were used. From visual inspection, the skeleton seemed of similar quality as skeletons from other studies using NODDI based GBSS [44, 45, 72]. This should however be investigated further by comparing the skeletons empirically, which will be done in the future. The threshold of the GM fraction is also chosen arbitrarily. In previous studies this threshold varies between 0.55 and 0.75 (here 0.55), the influence of this threshold on the results should also be investigated further.

Limitations and Future Work

One of the most obvious limitations is the quality of the skeleton, it is missing the top part of the brain. This is due to several subjects with cut-off scans. For our purposes, this is acceptable, since the top part of the brain (sensory-motor areas) is not heavily affected by AD in early stages. However, the missing top part of the skeleton should be resolved for more complete results. Apart from the missing part of the skeleton, the skeleton was also not compared to skeletons from already established methods [44, 52], due to time limitations. This will be done in the future.

While this thesis suggests, that GM and CSF fraction are more sensitive than MD, it still remains unclear, if it is also more sensitive than CTh. Further analysis will be needed, especially a statistical analysis corrected for CTh should be done to investigate the independent value of the tissue fractions.

Furthermore, the different statistical comparisons resulted in slightly different outcomes in some cases (e.g. GBSS and FreeSrufer region-based analysis of MD_{nocsf}). If the differences found by GBSS are actually significant or false positives should be confirmed by a larger study cohort.

Some other general limitations include the influence of partial volume effects and the lack of longitudinal comparisons. Even though GBSS was used to try to reduce the effect of partial volume effects, they cannot be ruled out completely. Furthermore, only cross-sectional data was used (i.e. one timepoint per subject). Therefore, it is not directly possible to make connections between disease progression and the tissue fractions (or any other metric). A longitudinal study in the future could give more insight on the usefulness of GM and CSF fraction as a biomarker to track disease progression.

7

Conclusion

The main goal of this thesis was to investigate methodological aspects that could lead to metrics sensitive to pathological processes occurring during the early stage of the AD pathological cascade. This was done by examining the microstructure of GM with the MT-CSD model.

This thesis demonstrates that GM and CSF fraction are promising biomarkers, that reflect expected microstructural changes during early stages of AD. The results suggest that GM and CSF fraction are more sensitive than MD to group differences, especially for A+T+ patients compared to healthy elderly. While the results seem promising, more work is needed to verify the results. The MT-CSD metrics need to be compared to other metrics to identify if they add unique information to the disease progression.

From both the analysis on empirical data and the simulations the use of the CSF correction employed appears questionable. By eliminating "CSF-like" signal, the analysis could have been biased since this step may have removed all the signal from tissue with high diffusivity.

Another contribution of this thesis is the adaption of GBSS to MT-CSD based metrics. The resulting skeleton looks comparable to skeletons emerging from NODDI-GBSS and the following statistical analysis yielded plausible results. This indicates a successful adaption, however direct comparisons to other GBSS pipelines are still pending.

Future work will include comparing GM and CSF fraction to cortical thickness to identify their potential value. Furthermore, the adapted GBSS pipeline will be compared to already established GBSS versions, to evaluate the quality and maybe advantages of the proposed alterations.

Bibliography

[1] J. L. Andersson and S. N. Sotiropoulos. "An integrated approach to correction for off-resonance effects and subject movement in diffusion MR imaging". *NeuroImage* **125** (2016), pp. 1063–1078. DOI: 10.1016/j.neuroimage.2015.10.019.

[2] J. L. Andersson et al. "How to correct susceptibility distortions in spin-echo echo-planar images: application to diffusion tensor imaging". *NeuroImage* **20**:2 (2003), pp. 870–888. DOI: 10.1016/S1053-8119(03)00336-7.

[3] J. L. Andersson et al. "Incorporating outlier detection and replacement into a non-parametric framework for movement and distortion correction of diffusion MR images". *NeuroImage* **141** (2016), pp. 556–572. DOI: 10.1016/j.neuroimage.2016.06.058.

[4] A. Arab et al. "Principles of diffusion kurtosis imaging and its role in early diagnosis of neurodegenerative disorders". *Brain Research Bulletin* **139** (2018), pp. 91–98. DOI: 10.1016/j.brainresbull.2018.01.015.

[5] J. Ashburner and K. J. Friston. "Voxel Based Morphometry". *Encyclopedia of Neuroscience* (2009), pp. 471–477. DOI: 10.1016/B978-008045046-9.00306-5.

[6] J. Ashburner and K. J. Friston. "Voxel-based morphometry - The methods". *NeuroImage* **11**:6 I (2000), pp. 805–821. DOI: 10.1006/nimg.2000.0582.

[7] B. Avants et al. "Advanced Normalization Tools (ANTS)". *Insight Journal* (2009), pp. 1–35.

[8] B. B. Avants et al. "A reproducible evaluation of ANTs similarity metric performance in brain image registration". *NeuroImage* **54**:3 (2011), pp. 2033–2044. DOI: 10.1016/J.NEUROIMAGE.2010.09.025.

[9] G. Ball et al. "Development of cortical microstructure in the preterm human brain". *Proceedings of the National Academy of Sciences of the United States of America* **110**:23 (2013), pp. 9541–9546. DOI: 10.1073/PNAS.1301652110/SUPPL_FILE/SM04.MOV.

[10] H. Braak and E. Braak. "Evolution of neuronal changes in the course of Alzheimer's disease". *Journal of Neural Transmission, Supplement* 53 (1998), pp. 127–140. DOI: 10.1007/978-3-7091-6467-9_11.

[11] H. Braak et al. “Staging of alzheimer-related cortical destruction”. *European Neurology* **33**:6 (1993), pp. 403–408. DOI: 10.1159/000116984.

[12] A. Chandra et al. “Magnetic resonance imaging in Alzheimer’s disease and mild cognitive impairment”. *Journal of Neurology* **266**:6 (2019), pp. 1293–1302. DOI: 10.1007/s00415-018-9016-3.

[13] H. Cho et al. “In vivo cortical spreading pattern of tau and amyloid in the alzheimer disease spectrum”. *Annals of neurology* **80**:2 (2016), pp. 247–258.

[14] L. Clerx et al. “New MRI Markers for Alzheimer’s Disease: A Meta-Analysis of Diffusion Tensor Imaging and a Comparison with Medial Temporal Lobe Measurements”. *Journal of Alzheimer’s Disease* **29**:2 (2012), pp. 405–429. DOI: 10.3233/JAD-2011-110797.

[15] J. Cohen. *Statistical Power Analysis for the Behavioral Sciences*. Routledge, 2013. DOI: 10.4324/9780203771587.

[16] S. Currie et al. “Understanding MRI: Basic MR physics for physicians”. *Postgraduate Medical Journal* **89**:1050 (2013), pp. 209–223. DOI: 10.1136/postgradmedj-2012-131342.

[17] F. Dell’Acqua and J. D. Tournier. “Modelling white matter with spherical deconvolution: How and why?” *NMR in Biomedicine* **32**:4 (2019). DOI: 10.1002/nbm.3945.

[18] M. Descoteaux. “High Angular Resolution Diffusion Imaging (HARDI)”. In: John Wiley and Sons, Inc., 2015, pp. 1–25. DOI: 10.1002/047134608x.w8258.

[19] R. S. Desikan et al. “An automated labeling system for subdividing the human cerebral cortex on mri scans into gyral based regions of interest”. *Neuroimage* **31**:3 (2006), pp. 968–980.

[20] T. Dhollander et al. “Improved white matter response function estimation for 3-tissue constrained spherical deconvolution”. *Proceedings of the 27th annual meeting of International Society of Magnetic Resonance in Medicine* (2019).

[21] T. Dhollander et al. “Unsupervised 3-tissue response function estimation from single-shell or multi-shell diffusion MR data without a co-registered T1 image Predicting stroke impairment using machine learning techniques View project A novel sparse partial correlation method fo”. *ISMRM Workshop on Breaking the Barriers of Diffusion MRI* **35**:September (2016), pp. 1–2.

[22] B. C. Dickerson et al. “The Cortical Signature of Alzheimer’s Disease: Regionally Specific Cortical Thinning Relates to Symptom Severity in Very Mild to Mild AD Dementia and is Detectable in Asymptomatic Amyloid-Positive Individuals”. *Cerebral Cortex* **19**:3 (2009), pp. 497–510. DOI: 10.1093/CERCOR/BHN113.

[23] A. Du et al. “Higher atrophy rate of entorhinal cortex than hippocampus in ad”. *Neurology* **62**:3 (2004), pp. 422–427.

[24] B. Dubois et al. “Research criteria for the diagnosis of alzheimer’s disease: revising the nincds–adrda criteria”. *The Lancet Neurology* **6**:8 (2007), pp. 734–746.

[25] B. Fischl and A. M. Dale. “Measuring the thickness of the human cerebral cortex from magnetic resonance images”. *Proceedings of the National Academy of Sciences* **97**:20 (2000), pp. 11050–11055.

[26] K. Gorgolewski et al. “Nipype: A flexible, lightweight and extensible neuroimaging data processing framework in Python”. *Frontiers in Neuroinformatics* **5** (2011), p. 13. DOI: 10.3389/FNINF.2011.00013/ABSTRACT.

[27] O. Hansson. “Biomarkers for neurodegenerative diseases”. *Nature Medicine* **27**:6 (2021), pp. 954–963. DOI: 10.1038/s41591-021-01382-x.

[28] J. Hardy and D. J. Selkoe. “The amyloid hypothesis of Alzheimer’s disease: progress and problems on the road to therapeutics”. *Science (New York, N.Y.)* **297**:5580 (2002), pp. 353–356. DOI: 10.1126/SCIENCE.1072994.

[29] J. Henf et al. “Mean diffusivity in cortical gray matter in Alzheimer’s disease: The importance of partial volume correction”. *NeuroImage: Clinical* **17** (2018), pp. 579–586. DOI: 10.1016/J.NICL.2017.10.005.

[30] C. R. Jack Jr et al. “Nia-aa research framework: toward a biological definition of alzheimer’s disease”. *Alzheimer’s & Dementia* **14**:4 (2018), pp. 535–562.

[31] B. Jeurissen and F. Szczepankiewicz. “Multi-tissue spherical deconvolution of tensor-valued diffusion MRI”. *NeuroImage* **245** (2021), p. 118717. DOI: 10.1016/J.NEUROIMAGE.2021.118717.

[32] B. Jeurissen et al. “Multi-tissue constrained spherical deconvolution for improved analysis of multi-shell diffusion MRI data”. *NeuroImage* **103** (2014), pp. 411–426. DOI: 10.1016/j.neuroimage.2014.07.061.

[33] S. Jillings et al. “Macro- And microstructural changes in cosmonauts’ brains after long-duration spaceflight”. *Science Advances* **6**:36 (2020). DOI: 10.1126/sciadv.aaz9488.

[34] R. L. Joie et al. “Prospective longitudinal atrophy in Alzheimer’s disease correlates with the intensity and topography of baseline tau-PET”. *Science Translational Medicine* **12**:524 (2020), p. 5732. DOI: 10.1126/SCITRANSLMED.AAU5732/SUPPL_FILE/AAU5732_SM.PDF.

[35] D. K. Jones and P. J. Basser. ““Squashing peanuts and smashing pumpkins”: How noise distorts diffusion-weighted MR data”. *Magnetic Resonance in Medicine* **52**:5 (2004), pp. 979–993. DOI: 10.1002/MRM.20283.

[36] E. Kellner et al. “Gibbs-ringing artifact removal based on local subvoxel-shifts”. *Magnetic Resonance in Medicine* **76**:5 (2016), pp. 1574–1581. DOI: 10.1002/mrm.26054. arXiv: 1501.07758.

[37] J. Kuhlmann et al. "CSF Aβ1–42 – an excellent but complicated Alzheimer's biomarker – a route to standardisation". *Clinica Chimica Acta* **467** (2017), pp. 27–33. DOI: 10.1016/J.CCA.2016.05.014.

[38] D. Le Bihan et al. "Diffusion tensor imaging: Concepts and applications". *Journal of Magnetic Resonance Imaging* **13**:4 (2001), pp. 534–546. DOI: 10.1002/JMRI.1076.

[39] A. Leuzy et al. "Diagnostic performance of ro948 f 18 tau positron emission tomography in the differentiation of alzheimer disease from other neurodegenerative disorders". *JAMA neurology* **77**:8 (2020), pp. 955–965.

[40] X. Li et al. "Gray matter concentration and effective connectivity changes in alzheimer's disease: a longitudinal structural mri study". *Neuroradiology* **53**:10 (2011), pp. 733–748.

[41] N. Mattsson et al. "Staging β-amyloid pathology with amyloid positron emission tomography". *JAMA neurology* **76**:11 (2019), pp. 1319–1329.

[42] M. A. Mintun et al. "Donanemab in Early Alzheimer's Disease". *New England Journal of Medicine* **384**:18 (2021), pp. 1691–1704. DOI: 10.1056/nejmoa2100708.

[43] R. Mito et al. "In vivo microstructural heterogeneity of white matter lesions in healthy elderly and Alzheimer's disease participants using tissue compositional analysis of diffusion MRI data". *NeuroImage: Clinical* **28** (2020), p. 102479. DOI: 10.1016/j.nicl.2020.102479.

[44] A. Nazeri et al. "Functional consequences of neurite orientation dispersion and density in humans across the adult lifespan". *Journal of Neuroscience* **35**:4 (2015), pp. 1753–1762. DOI: 10.1523/JNEUROSCI.3979-14.2015.

[45] A. Nazeri et al. "Gray Matter Neuritic Microstructure Deficits in Schizophrenia and Bipolar Disorder". *Biological Psychiatry* **82**:10 (2017), pp. 726–736. DOI: 10.1016/J.BIOPSYCH.2016.12.005.

[46] M. Nilsson et al. "An open-source framework for analysis of multidimensional diffusion MRI data implemented in MATLAB." *Proc Intl Soc Mag Reson Med* June (2018), pp. 1–3. 35.

[47] R. Ossenkoppele et al. "Accuracy of Tau Positron Emission Tomography as a Prognostic Marker in Preclinical and Prodromal Alzheimer Disease: A Head-to-Head Comparison Against Amyloid Positron Emission Tomography and Magnetic Resonance Imaging". *JAMA Neurology* **78**:8 (2021), pp. 961–971. DOI: 10.1001/JAMANEUROL.2021.1858.

[48] S. Palmqvist et al. "Discriminative accuracy of plasma phospho-tau217 for alzheimer disease vs other neurodegenerative disorders". *Jama* **324**:8 (2020), pp. 772–781.

[49] S. Palmqvist et al. "Earliest accumulation of β-amyloid occurs within the default-mode network and concurrently affects brain connectivity". *Nature communications* **8**:1 (2017), pp. 1–13.

[50] S. Palmqvist et al. "Performance of Fully Automated Plasma Assays as Screening Tests for Alzheimer Disease–Related β-Amyloid Status". *JAMA Neurology* **76**:9 (2019), pp. 1060–1069. DOI: 10.1001/JAMANEUROL.2019.1632.

[51] T. D. Parker et al. "Cortical microstructure in young onset Alzheimer's disease using neurite orientation dispersion and density imaging". *Human Brain Mapping* **39**:7 (2018), pp. 3005–3017. DOI: 10.1002/hbm.24056.

[52] P. Parvathaneni et al. "Gray matter surface based spatial statistics (GS-BSS) in diffusion microstructure". In: vol. 10433 LNCS. Springer, Cham, 2017, pp. 638–646. DOI: 10.1007/978-3-319-66182-7_73.

[53] M. J. Pontecorvo et al. "A multicentre longitudinal study of flortaucipir (18F) in normal ageing, mild cognitive impairment and Alzheimer's disease dementia". *Brain* **142**:6 (2019), pp. 1723–1735. DOI: 10.1093/brain/awz090.

[54] Y. Rathi et al. "Gray matter alterations in early aging: A diffusion magnetic resonance imaging study". *Human Brain Mapping* **35**:8 (2014), pp. 3841–3856. DOI: 10.1002/hbm.22441.

[55] E. Rodriguez-Vieitez et al. "Association of cortical microstructure with amyloid-β and tau: impact on cognitive decline, neurodegeneration, and clinical progression in older adults". *Molecular psychiatry* (2021), pp. 1–10.

[56] S. E. Rose et al. "Gray and white matter changes in Alzheimer's disease: A diffusion tensor imaging study". *Journal of Magnetic Resonance Imaging* **27**:1 (2008), pp. 20–26. DOI: 10.1002/JMRI.21231.

[57] E. Scola et al. "A diffusion tensor mri study of patients with mci and ad with a 2-year clinical follow-up". *Journal of Neurology, Neurosurgery & Psychiatry* **81**:7 (2010), pp. 798–805.

[58] J. G. Sled et al. "A nonparametric method for automatic correction of intensity nonuniformity in MRI data". *IEEE transactions on medical imaging* **17**:1 (1998), pp. 87–97. DOI: 10.1109/42.668698.

[59] S. M. Smith and T. E. Nichols. "Threshold-free cluster enhancement: addressing problems of smoothing, threshold dependence and localisation in cluster inference". *NeuroImage* **44**:1 (2009), pp. 83–98. DOI: 10.1016/J.NEUROIMAGE.2008.03.061.

[60] S. M. Smith et al. "Advances in functional and structural MR image analysis and implementation as FSL". In: *NeuroImage*. Vol. 23. SUPPL. 1. 2004. DOI: 10.1016/j.neuroimage.2004.07.051.

[61] S. M. Smith et al. "Tract-based spatial statistics: Voxelwise analysis of multi-subject diffusion data". *NeuroImage* **31**:4 (2006), pp. 1487–1505. DOI: 10.1016/J.NEUROIMAGE.2006.02.024.

[62] C. Sur et al. "BACE inhibition causes rapid, regional, and non-progressive volume reduction in Alzheimer's disease brain". *Brain* **143**:12 (2020), pp. 3816–3826. DOI: 10.1093/BRAIN/AWAA332.

[63] S. J. Teipel et al. "Anatomical MRI and DTI in the Diagnosis of Alzheimer's Disease: A European Multicenter Study". *Journal of Alzheimer's Disease* **31**:s3 (2012), S33–S47. DOI: 10.3233/JAD-2012-112118.

[64] J. D. Tournier et al. "Direct estimation of the fiber orientation density function from diffusion-weighted MRI data using spherical deconvolution". *NeuroImage* **23**:3 (2004), pp. 1176–1185. DOI: 10.1016/J.NEUROIMAGE.2004.07.037.

[65] J. D. Tournier et al. "MRtrix3: A fast, flexible and open software framework for medical image processing and visualisation". *NeuroImage* **202** (2019), p. 116137. DOI: 10.1016/J.NEUROIMAGE.2019.116137.

[66] J. D. Tournier et al. "Robust determination of the fibre orientation distribution in diffusion MRI: Non-negativity constrained super-resolved spherical deconvolution". *NeuroImage* **35**:4 (2007), pp. 1459–1472. DOI: 10.1016/J.NEUROIMAGE.2007.02.016.

[67] N. J. Tustison et al. "N4ITK: improved N3 bias correction". *IEEE transactions on medical imaging* **29**:6 (2010), pp. 1310–1320. DOI: 10.1109/TMI.2010.2046908.

[68] G. E. Uhlenbeck and L. S. Ornstein. "On the Theory of the Brownian Motion". *Physical Review* **36**:5 (1930), p. 823. DOI: 10.1103/PhysRev.36.823.

[69] J. Veraart et al. "Diffusion MRI noise mapping using random matrix theory". *Magnetic Resonance in Medicine* **76**:5 (2016), pp. 1582–1593. DOI: 10.1002/mrm.26059.

[70] V. L. Villemagne et al. "Amyloid β deposition, neurodegeneration, and cognitive decline in sporadic Alzheimer's disease: a prospective cohort study". *The Lancet Neurology* **12**:4 (2013), pp. 357–367. DOI: 10.1016/S1474-4422(13)70044-9.

[71] J. W. Vogel et al. "Spread of pathological tau proteins through communicating neurons in human alzheimer's disease". *Nature communications* **11**:1 (2020), pp. 1–15.

[72] N. M. Vogt et al. "Cortical Microstructural Alterations in Mild Cognitive Impairment and Alzheimer's Disease Dementia". *Cerebral Cortex* **30**:5 (2020), pp. 2948–2960. DOI: 10.1093/cercor/bhz286.

[73] P. S. Weston et al. "Diffusion imaging changes in grey matter in Alzheimer's disease: A potential marker of early neurodegeneration". *Alzheimer's Research and Therapy* **7**:1 (2015), pp. 1–8. DOI: 10.1186/s13195-015-0132-3.

[74] P. S. Weston et al. "Measuring cortical mean diffusivity to assess early microstructural cortical change in presymptomatic familial Alzheimer's disease". *Alzheimer's Research and Therapy* **12**:1 (2020), pp. 1–10. DOI: 10.1186/S13195-020-00679-2/FIGURES/4.

[75] J. L. Whitwell. "Voxel-Based Morphometry: An Automated Technique for Assessing Structural Changes in the Brain". *Journal of Neuroscience* **29**:31 (2009), pp. 9661–9664. DOI: 10.1523/JNEUROSCI.2160-09.2009.

[76] A. M. Winkler et al. "Permutation inference for the general linear model". *NeuroImage* **92** (2014), pp. 381–397. DOI: 10.1016/J.NEUROIMAGE.2014.01.060.

[77] H. Zhang et al. "NODDI: Practical in vivo neurite orientation dispersion and density imaging of the human brain". *NeuroImage* **61**:4 (2012), pp. 1000–1016. DOI: 10.1016/j.neuroimage.2012.03.072.

A

Image artifacts

MR images have several known artifacts that originate in the image acquisition and reconstruction. These can be corrected to improve the image quality and any following analysis. The corrections used in this thesis are described in the following section, this is however not an exhaustive list of all artifacts and corrections. This chapter is supposed to give a rough overview of the methods and concepts, not a detailed explanation of every method. For more in-depth explanations the reader is referred to the referenced publications [2, 1, 36, 69, 67].

A.1 Denoising

The first preprocessing step is to remove noise from the images. When fitting diffusion models to the data, it is especially relevant to denoise the images, as the Rician distribution of the noise biases the diffusion parameters [35]. The most common method used for denoising is MP-PCA (Marchenko-Pastur principal component analysis) [69]. The signal is transformed into the PCA domain, where the noise is given by the Marchenko-Pastur distribution, which is a closed distribution (contrary to a Gaussian distribution with infinitely long tails). With the MP distribution, the noise level can be determined and filtered by setting thresholds (λ_-, λ_+) on the eigenvalues. The noise distribution in the PCA domain is shown in Figure A.1. It is important to implement denoising as the first step in the preprocessing pipeline, as the next steps can corrupt the noise leading to non-Gaussian properties.

A.2 Gibbs Artifact Removal

Gibbs-ringing is an artifact that occurs near sharp image gradients at tissue boundaries as spurious oscillations. This artifact is caused by the truncated (i.e. discrete) sampling of the k-space. This grid-like sampling of the k-space is equivalent to a convolution with a sinc-function in the image domain. On sharp edges, this leads to oscillations in the reconstruction. The strength of this oscillation (i.e. ringing) effect depends on the relative location of the edge to the sampling grid. In the worst case, the samples are taken at the maxima of the sinc-function, leading to the maximal

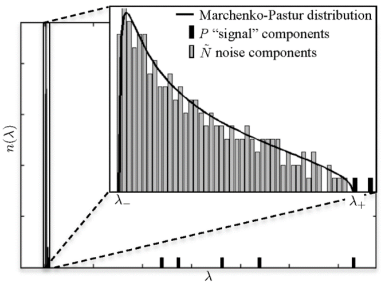

Figure A.1 Eigenvalue spectrum of DW data. The noise components follow an MP-distribution and can be filtered out by setting a threshold on the eigenvalues. Image from [69].

amplitude of the ringing. When sampled at the zero-crossing of the sinc-function the ringing disappears (see Figure A.2). To remove the Gibbs ringing, local sub-voxel shifts are used to sample the sinc-pattern at its zero-crossing [36]. This is done by finding the optimal voxel-shift for each voxel that minimizes the oscillations in its neighborhood.

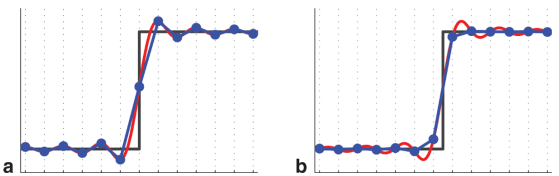

Figure A.2 Reconstruction of an image with an edge (black) with discrete sampling. The reconstructed image (blue) shows oscillations near the edge (Gibbs ringing) if it is sampled at the maxima (**a**) of the sinc-function (red) and no oscillations if sampled at the zero-crossings (**b**). To remove the Gibbs ringing, sub-voxel shifts are used to always sample at the zero-crossings. Image from [36].

A.3 Susceptibility-induced Distortions Correction

A problem occurring with diffusion weighted images is geometric and intensity distortions caused by local gradients near junctions of tissues of different magnetic susceptibility. This leads to distorted diffusion tensors, this should especially be corrected if one is interested in the geometry of the brain. These distortions can be estimated by obtaining two images for each diffusion gradient in opposite directions. These two images will exhibit the same distortions in magnitude, just in

opposite directions. With these images and the information about the image acquisitions process, the field inhomogeneities can be estimated and corrected [2]. Often, the susceptibility field is just estimated in this step and corrected for in the next step, together with the eddy current and motion correction.

A.4 Motion and Eddy Correction

Two other important artifacts that need to be corrected are motion artifacts and eddy current (EC) artifacts. These are corrected in one integrated approach [1]. Motion artifacts are caused by (involuntary) movement of the subject during the scan. Eddy currents are induced by a changing magnetic field, which is always the case in MR. These eddy currents cause time-varying gradients and shifts in the magnetic field which lead to blurring, shading, ghosting effects and misregistration of the images. To correct for these artifacts an iterative algorithm is applied, where each iteration consists of two steps: the prediction step and the estimation step. The main idea is to predict what the data should look like and compare this prediction to the observed data. The error is then used to update the EC field and movement estimation. The susceptibility field can be incorporated in this approach, so the data only needs to be resampled once to correct for all three artifacts. An overview of this algorithm is given in Figure A.3, for more details on each step the reader is referred to [1].

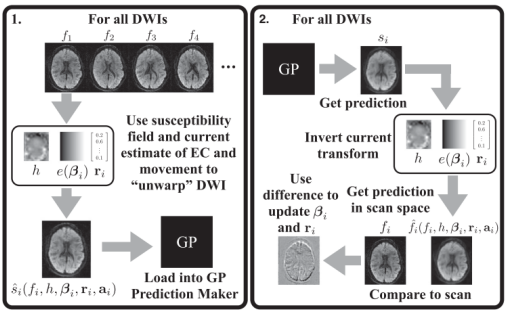

Figure A.3 The correction algorithm for eddy current- and susceptibility-induced distortions as well as subject movement. The algorithm is run for 5 iterations. Image from [1] (for more information on the exact steps the reader is referred to this publication).

A.5 Bias Field Correction

The bias field is a low-frequency intensity non-uniformity in the images. The intensity varies smoothly across the image, which can impact automated segmentation,

estimations of model parameters and ultimately statistical analysis, so it should be corrected. An example of a bias field correction can be seen in Figure A.4. The correction of the bias field is done by estimating the bias field based on the intensities of the image, smoothed and compared to earlier field estimates. This iterative process is stopped once the field converges. The image is then corrected by dividing the original image with the estimated bias field, leading to uniform intensities across the image. This algorithm was first developed by [58] and then further improved by [67].

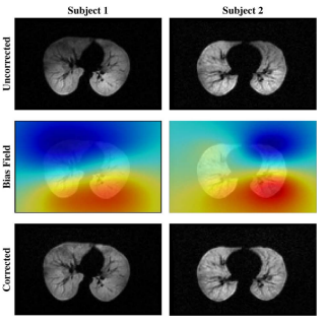

Figure A.4 Example of a bias field correction on a lung MRI. Top: uncorrected images. Middle: estimated bias fields. Bottom: corrected images. Figure from [67].

B

Additional results

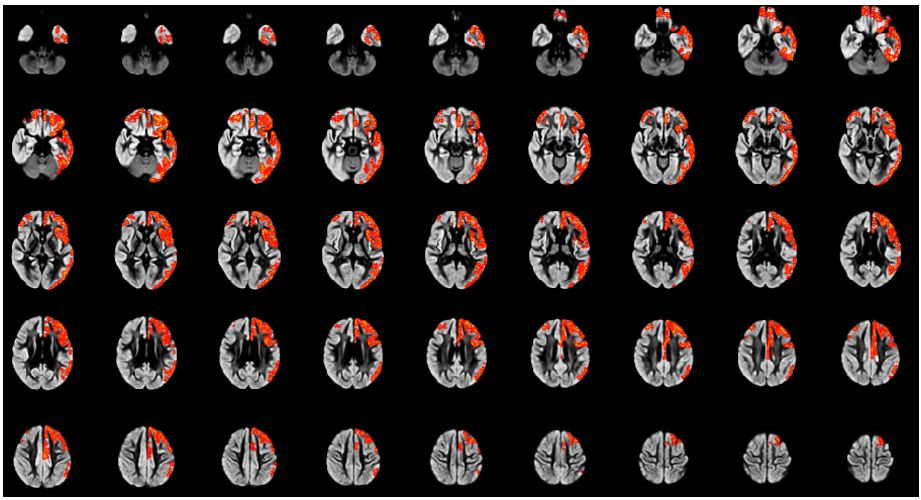

Figure B.1 GM fraction A-T- vs A+T-.

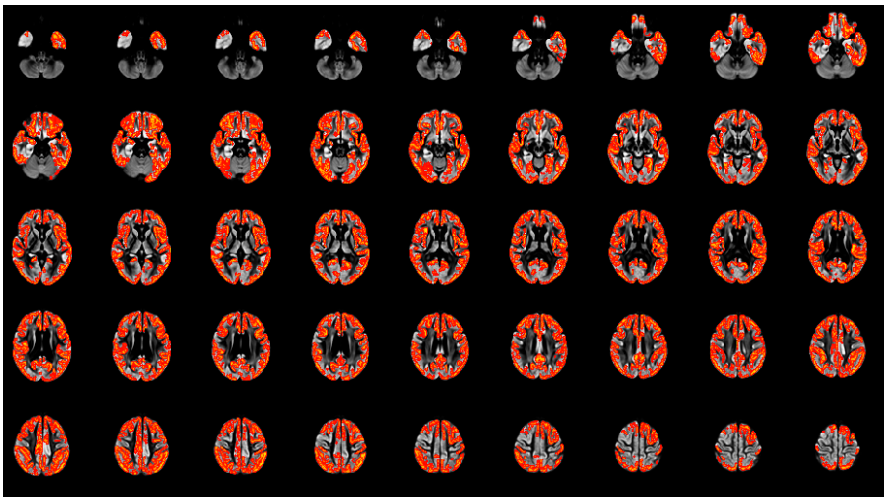

Figure B.2 GM fraction A-T- vs A+T+.

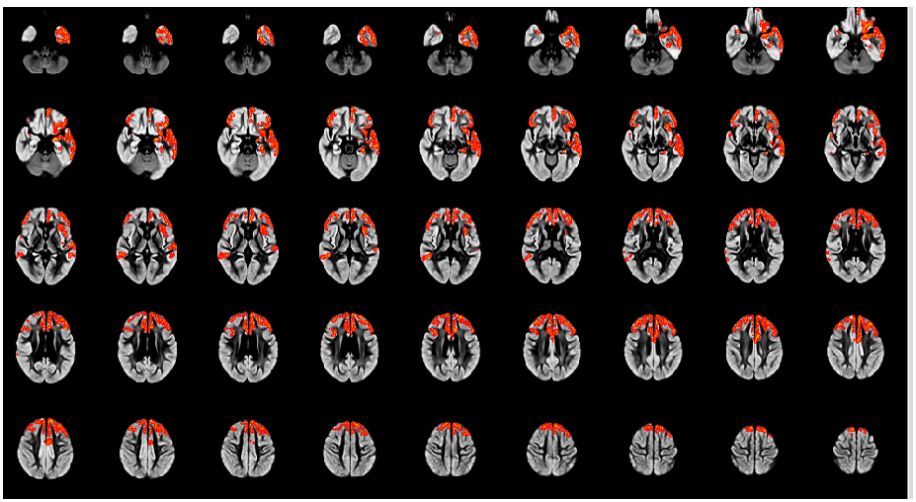

Figure B.3 CSF fraction A-T- vs A+T-.

Lund University
Department of Automatic Control
Box 118
SE-221 00 Lund Sweden

Document name
MASTER'S THESIS

Date of issue
May 2022

Document Number
TFRT-6160

Author(s)
Teresa Scheidt

Supervisor
Markus Nilsson, Department of Clinical Sciences, Lund University, Sweden
Nicola Spotorno, Department of Clinical Sciences, Lund University, Sweden
Kristian Soltesz, Dept. of Automatic Control, Lund University, Sweden (examiner)

Title and subtitle
Probing Gray Matter Microstructure in Alzheimer's Disease using Diffusion MRI

Abstract

Alzheimer's disease is a neurodegenerative disease and the most common cause of dementia. Apart from an early and accurate diagnosis, the ability to track progressive changes is important for the development of disease modifying treatments. Diffusion magnetic resonance imaging is a potential method to detect the microstructural changes in the gray matter, which appear years prior to cortical atrophy and clinical symptoms.

In this thesis, multi-tissue constrained spherical deconvolution is used to model three main tissue classes in the brain (gray matter, white matter and cerebral spinal fluid) based on the diffusion signal. By comparing the tissue fractions in healthy elderly with patients in different stages of the Alzheimer's disease spectrum using gray matter based spatial statistics, this work demonstrates the potential of the tissue fractions to investigate microstructural changes. The gray matter fraction was lower in patients on the AD spectrum, while the cerebral spinal fluid fraction was higher. These differences are in line with the expected results and appear in pathological affected areas. Compared to another diffusion based metric (mean diffusivity) the tissue fractions showed a higher sensitivity and detected differences in an earlier stage. Overall, this indicates the high potential of these metrics to detect early microstructural changes in Alzheimer's disease.

Keywords

Classification system and/or index terms (if any)

Supplementary bibliographical information

ISSN and key title
0280-5316

ISBN

Language
English

Number of pages
1-67

Recipient's notes

Security classification

http://www.control.lth.se/publications/